Computer Modeling in Engineering & Sciences

Tech Science Press

Doi:10.32604/cmes.2025.064815

ARTICLE

Analysis of a Laplace Spectral Method for Time-Fractional Advection-Diffusion Equations Incorporating the Atangana-Baleanu Derivative

Kamran[1,*], Farman Ali Shah[1], Kallekh Afef[2], J. F. Gómez-Aguilar[3], Salma Aljawi[4] and Ioan-Lucian Popa[5,6,*]

[1]Department of Mathematics, Islamia College Peshawar, Peshawar, Khyber Pakhtoon Khwa, 25120, Pakistan
[2]Department of Mathematics, College of Science, King Khalid University, Abha, 61413, Saudi Arabia
[3]Centro de Investigación en Ingenierìa y Ciencias Aplicadas (CIICAp-IICBA)/UAEM, Universidad Autónoma del Estado de Morelos, Av. Universidad 1001. Col. Chamilpa, Cuernavaca, 62209, Morelos, México
[4]Department of Mathematical Sciences, Princess Nourah Bint Abdulrahman University, Riyadh, 11671, Saudi Arabia
[5]Department of Computing, Mathematics and Electronics, "1 Decembrie 1918" University of Alba Iulia, Alba Iulia, 510009, Romania
[6]Faculty of Mathematics and Computer Science, Transilvania University of Brasov, Iuliu Maniu Street 50, Brasov, 500091, Romania

*Corresponding Authors: Kamran. Email: kamran.maths@icp.edu.pk; Ioan-Lucian Popa. Email: lucian.popa@uab.ro

Received: 25 February 2025; Accepted: 07 May 2025; Published: 30 June 2025

ABSTRACT: In this article, we develop the Laplace transform (LT) based Chebyshev spectral collocation method (CSCM) to approximate the time fractional advection-diffusion equation, incorporating the Atangana-Baleanu Caputo (ABC) derivative. The advection-diffusion equation, which governs the transport of mass, heat, or energy through combined advection and diffusion processes, is central to modeling physical systems with nonlocal behavior. Our numerical scheme employs the LT to transform the time-dependent time-fractional PDEs into a time-independent PDE in LT domain, eliminating the need for classical time-stepping methods that often suffer from stability constraints. For spatial discretization, we employ the CSCM, where the solution is approximated using Lagrange interpolation polynomial based on the Chebyshev collocation nodes, achieving exponential convergence that outperforms the algebraic convergence rates of finite difference and finite element methods. Finally, the solution is reverted to the time domain using contour integration technique. We also establish the existence and uniqueness of the solution for the proposed problem. The performance, efficiency, and accuracy of the proposed method are validated through various fractional advection-diffusion problems. The computed results demonstrate that the proposed method has less computational cost and is highly accurate.

KEYWORDS: Laplace transform; spectral method; existence theory; fractional derivative with non-singular kernel; contour integration methods

1 Introduction

Fractional calculus (FC) is a historical discipline in mathematics that traces its origins to the works of Leibniz and Euler, who explored integrals and derivatives of non-integer orders [1]. Despite significant advancements, this topic continues to captivate researchers due to its rich mathematical and numerical aspects. Today, FC extends beyond pure mathematics and has found applications in various scientific disciplines [2]. Replacing standard operators with fractional operators has significantly enhanced the precision and accuracy of numerous physical models and systems [3–5]. Researchers have explored numerous fractional operators and assessed various definitions of fractional derivatives, particularly those governed

by power-law kernels, commonly known as singular or local fractional derivatives. Notable examples include the Grünwald-Letnikov, Riemann-Liouville, Caputo, Riesz, and Hadamard fractional derivatives [6]. However, these fractional derivatives can efficiently model the non-local and dissipative properties of physical processes. The non-locality of a fractional derivative refers to the fact that the value of a fractional derivative at a given point depends on the function's values over an entire interval rather than just at the point itself.

In 2015, Caputo and Fabrizio [7] introduced a new fractional derivative, termed the Caputo-Fabrizio (CF) derivative, which employs an exponential kernel to overcome the limitations of fractional derivatives with singular kernels, such as those found in the Riemann-Liouville and Liouville-Caputo derivatives. The singularity in these earlier definitions often complicates their application to physical systems. The CF derivative's exponential kernel, being nonsingular, provides a more natural transition and eliminates the issues associated with the Riemann-Liouville and Liouville-Caputo derivatives. However, despite its innovation, the CF derivative faced criticisms for a notable drawback: its kernel lacks nonlocality. To address these shortcomings, Atangana and Baleanu [8] introduced a novel fractional derivative in 2016, known as Atangana-Baleanu (AB) derivative, which is based on the Mittag-Leffler function. Unlike the CF derivative the AB derivative incorporates a nonlocal and nonsingular kernel, effectively combining the strengths of the Riemann-Liouville, Liouville-Caputo, and Caputo-Fabrizio derivatives. The AB derivative provides several advantages: (i) its nonlocal nature guarantees that it captures the full historical behavior of the function being differentiated; (ii) it has an adjustable parameter, that lets researchers change the fractional order to enhance data-fitting accuracy; (iii) the AB derivative exhibits greater flexibility than its predecessor's derivatives, enabling accurate modeling of complex systems; and (iv) it offers a unifying structure that can refine and improve the existing models across various scientific domains by integrating the features of the Riemann-Liouville, Liouville-Caputo and extending their applicability. Due to these compelling attributes, the AB derivative has gained significant attention and has been successfully applied to a wide range of real-world problems [9].

Time-fractional advection-diffusion equations (TFADEs) are widely used models in applied mathematics to describe various physical systems. The advection term represents the movement of a fluid along a concentration gradient, while the diffusion term describes the process by which material spreads from regions of higher to lower concentration over time. TFADEs are applied to transport processes, including the long-range dispersion of air pollutants [10], turbulence [11], water transport in soil [12], dispersion in porous media [13], shallow water flow [14], ion transport in heterogeneous media [15], blood flow with chemical interactions [16], and contaminant transport in soil [17].

Analytical solutions for TFADEs have been derived by various researchers. For example, Sanskrityayn and Kumar [18] derived analytical solutions to TFADEs using Green's function methods. Avci and Yetim [19] obtained analytical solutions for TFADEs incorporating the Atangana-Baleanu fractional derivative, while Mirza and Vieru [20] derived fundamental solutions for TFADEs using the Caputo-Fabrizio derivative. However, obtaining exact solutions for TFADEs is often challenging due to the involvement of complex functions, which can be difficult to handle analytically.

As a result, developing accurate and efficient numerical schemes has become essential. Many authors in the literature have proposed numerical solutions for TFADEs. Umer et al. [21] analyzed numerical solutions of advection-diffusion equations with the Atangana-Baleanu fractional derivative using an extended cubic B-spline technique. Fazio et al. [22] studied a finite difference method on non-uniform meshes for TFADEs with a source term. Ahmed et al. [23] applied a Haar wavelet-based numerical technique to solve TFADEs. Kamran et al. [24] investigated numerical inverse Laplace transform methods for approximating TFADEs.

Other contributions include the work by Pareek et al. [25], who developed the natural transform method for solving TFADEs, and Chawla et al. [26], who utilized extended one-step time integration schemes. Liu et al. [27] proposed a radial basis function (RBF)-based differential quadrature method for solving two-dimensional TFADEs. Nguyen and Reynen [28] devised a space-time least squares finite element scheme for approximating TFADEs, while Cunha et al. [29] employed the boundary element method to solve TFADEs. Sweilam et al. [30] simulated TFADEs using a spectral collocation method combined with a non-standard finite difference technique.

Many authors have developed and modified numerical methods for the approximation of fractional partial differential equations (FPDEs) from various perspectives, focusing on improving accuracy, stability, efficiency, consistency, and performance in terms of computational cost. In recent years, hybrid methods have gained significant attention due to their high accuracy, low computational cost, and ease of implementation for discretizing FPDEs.

Hybrid methods combine two or more approaches, enabling them to mitigate the limitations of individual methods. As a result, hybrid methods can approximate complex problems in a simple and effective manner. In the literature, several researchers have proposed hybrid methods. For example, Yin et al. [31] combined the Laplace transform and Legendre wavelet methods for the numerical simulation of Klein-Gordon equations. Soares and Mansur [32] coupled the boundary element method with the finite element method for solving acoustic elastodynamic problems. A hybrid method based on the Laplace transform and Legendre wavelet approaches was analyzed in [33] for the approximation of Lane-Emden equations. Khan et al. [34] combined the homotopy perturbation method with the Laplace transform method to solve fractional models. Joujehi et al. [35] developed a hybrid method based on Beta functions and fractional-order Bernoulli wavelets for approximating multi-term TFPDEs in fluid mechanics. A review of the Jacobi-Galerkin spectral method for linear partial differential equations is examined by Hafez and Youssri [36]. Lim and Li [37] coupled the boundary element method with the finite difference method to approximate fluid-structure interaction problems with dynamic analysis of outer hair cells. Kamran et al. [38] combined the Laplace transform with radial basis functions for the numerical approximation of the mobile-immobile advection-dispersion problem arising in solute transport. Sahu and Jena [39] developed an efficient technique for time fractional Klein-Gordon equation based on modified Laplace Adomian decomposition technique via hybridized Newton-Raphson Scheme arises in relativistic fractional quantum mechanics.

The main objective of this work is to develop and analyze a hybrid Laplace Transform-based Chebyshev Spectral Collocation Method (LT-CSCM) for the efficient numerical solution of time-fractional advection-diffusion equations (TFADEs) featuring a nonsingular kernel. By combining the LT for temporal discretization with the CSCM for spatial discretization, our method aims to achieve high accuracy and computational efficiency.

The CSCM is a subclass of spectral methods that has recently garnered significant attention due to its straightforward implementation for the spatial approximation of fractional partial differential equations (FPDEs). Within the numerical framework for FPDEs, CSCM belongs to the family of Weighted Residual Methods (WRMs) [40]. This family includes the Tau, Galerkin, and collocation methods, each employing distinct techniques to minimize residuals. In the Galerkin and Tau methods, residuals are projected onto a polynomial space and constrained to be zero, while the collocation method enforces zero residuals at specific grid points. For FPDEs, Chebyshev collocation points are highly effective as grid points due to their optimal distribution, which enhances numerical accuracy. CSCM utilizes basis functions, typically Lagrange interpolation polynomials, defined at these points [41]. This global approach achieves spectral convergence, delivering high accuracy for problems with simple geometries and smooth solutions [42,43].

Compared to finite difference or finite element methods, CSCM is easier to implement and significantly reduces computational cost.

The CSCMs have been widely adopted by numerous researchers for many applications. Such as Khader and Saad [44] utilized the CSCM for the solution of the fractional Fisher problems. In [45], the authors proposed approximating fractional-order diffusion problems using CSCM combined with a power-series method based on residuals. The authors of [46] obtained the solution of the time-fractional advection-diffusion equation using CSCM. Tohidi [47] developed a numerical scheme for finding approximate solutions of one-dimensional parabolic partial differential equations (PDEs) under non-classical boundary conditions. In [48], the authors proposed a spectral collocation method based on differentiated Chebyshev polynomials to obtain numerical solutions for various types of nonlinear partial differential equations. Li et al. [49] employed the CSCM to solve the transport equation with given initial and boundary conditions. Rongpei et al. [50] solved two-dimensional nonlinear reaction-diffusion equations with Neumann boundary conditions using a new highly accurate CSCM.

The LT is an efficient and error-free method for the temporal discretization of FPDEs, addressing stability issues often encountered with traditional time-marching methods. These methods are stable and accurate only if the error calculated in a one-time step does not amplify as computations progress. In other words, time-marching methods remain stable if the error diminishes or remains unchanged during computations. Moreover, achieving optimal accuracy with time-marching methods typically requires smaller time steps, which significantly increases computational cost [51], thus affecting the overall efficiency of the method. One of its key advantages is its ability to convert differential equations into algebraic equations, making complex problems more manageable. Additionally, it provides a systematic approach for handling initial conditions directly within the transformed domain, avoiding the need for numerical time-stepping methods that may suffer from stability issues [52]. The LT is particularly beneficial for solving linear time-invariant systems and fractional differential equations, as it allows for analytical solutions in many cases [53]. However, the method also has limitations. It is less effective for nonlinear problems, as transforming the nonlinear terms is not straightforward, often requiring approximations or numerical techniques [54]. By employing the LT for temporal discretization, the FPDEs are transformed into the Laplace domain. To obtain the solution in the time domain, the inverse Laplace transform (ILT) must be applied. However, the exact computation of Evaluating the Bromwich integral is computationally complex, prompting the adoption of numerical inverse Laplace transform methods (ILTMs). Several authors have developed numerical ILTMs. For instance: De Hoog et al. [55] employed the quotient-difference scheme to formulate an improved ILTM that accelerates Fourier series convergence. Stehfest [56] developed a linear acceleration method using Salzer's approach for numerical inversion of the LT. Talbot [57] introduced an efficient ILTM. Weideman and Trefethen [58] utilized parabolic and hyperbolic contours to approximate the Bromwich integral. Weeks [59] employed Laguerre functions for numerical ILTM. Each numerical method for inverting the Laplace transform has specific applications and is best suited to a particular problem. Contour integration methods, such as those based on hyperbolic, parabolic, or Talbot contours, are particularly effective for partial differential equations (PDEs) due to their ease of implementation and high accuracy. These methods deform the integration path in the complex plane to optimize convergence, minimizing computational complexity while maintaining precision. In this work, we utilize the numerical ILTMs described in [58,60]. Consider the following 2-D TFADE:

$$\begin{cases} \partial_\tau^\sigma \mathrm{u}(\bar{\boldsymbol{x}},\tau) &= \mathfrak{L}\mathrm{u}(\bar{\boldsymbol{x}},\tau) + \xi(\bar{\boldsymbol{x}},\tau), \quad (\bar{\boldsymbol{x}},\tau) \in \Theta \times [0,1], \\ \mathfrak{B}\mathrm{u}(\bar{\boldsymbol{x}},\tau) &= \zeta(\bar{\boldsymbol{x}},\tau), \quad \bar{\boldsymbol{x}} \in \partial\Theta, \\ \mathrm{u}(\bar{\boldsymbol{x}},0) &= \mathrm{u}_0, \end{cases} \tag{1}$$

where, $\bar{\boldsymbol{x}} = (x, y) \in \Theta = [-1,1]^2 \subset \mathbb{R}^2$, $\partial\Theta$ is the bound of Θ, $\mathfrak{L}$ is the linear differential operator $\mathfrak{L}\mathrm{u}(\bar{\boldsymbol{x}}, \tau) = a_1\Delta\mathrm{u}(\bar{\boldsymbol{x}}, \tau) - a_2\nabla\mathrm{u}(\bar{\boldsymbol{x}}, \tau)$, with a_1, a_2 positive constants, $\mathfrak{B}$ a linear boundary operator, $\xi(\bar{\boldsymbol{x}}, \tau)$, $\zeta(\bar{\boldsymbol{x}}, \tau)$ continuous functions, and the Atangana-Baleanu-Caputo (ABC) time-fractional derivative of order $\sigma \in [0,1]$ defined as [8]

$$\partial_\tau^\sigma \mathrm{u}(\bar{\boldsymbol{x}}, \tau) = \frac{\mathrm{B}(\sigma)}{1-\sigma}\int_0^\tau \partial_s \mathrm{u}(\bar{\boldsymbol{x}}, s)\mathrm{E}_\sigma\left(\frac{-\sigma(\tau - s)^\sigma}{1-\sigma}\right)ds, \tag{2}$$

with

$$\mathrm{B}(\sigma) = \frac{\sigma}{\Gamma(\sigma)} + (1-\sigma),$$

and $\mathrm{E}_\sigma(.)$ the Mittag-Leffler function defined as

$$\mathrm{E}_\sigma(\tau) = \sum_{r=0}^{\infty}\frac{\tau^r}{\Gamma(r\sigma+1)},\ \sigma > 0,\ \tau \in (-\infty, \infty). \tag{3}$$

2 Existence and Uniqueness of the Solution

In this section, we utilize the fixed-point theory to prove the existence and uniqueness of the solution to the fractional advection-diffusion model (1). Let us define a Banach space $C(\Lambda, \mathbb{R})$ of continuous functions from $\Lambda = \Theta \times [0,1]$ into $\mathbb{R}$, equipped with the norm defined by $\|\mathrm{u}\|_\infty := \sup\{|\mathrm{u}(\bar{\boldsymbol{x}}, \tau)|; (\bar{\boldsymbol{x}}, \tau) \in \Lambda\}$. By applying the AB-fractional integral operator to (1), we obtain

$$\begin{aligned}\mathrm{u}(\bar{\boldsymbol{x}}, \tau) &= \mathrm{u}_0 + \frac{1-\sigma}{\mathrm{B}(\sigma)}\Big(a_1\Delta\mathrm{u}(\bar{\boldsymbol{x}}, \tau) - a_2\nabla\mathrm{u}(\bar{\boldsymbol{x}}, \tau) + \xi(\bar{\boldsymbol{x}}, \tau)\Big) \\ &\quad + \frac{\sigma}{\Gamma(\sigma)\mathrm{B}(\sigma)}\int_0^\tau (\tau - s)^{\sigma-1}\Big(a_1\Delta\mathrm{u}(\bar{\boldsymbol{x}}, \tau) - a_2\nabla\mathrm{u}(\bar{\boldsymbol{x}}, \tau) + \xi(\bar{\boldsymbol{x}}, \tau)\Big)ds.\end{aligned} \tag{4}$$

Let define the operator $\mathrm{X} : C(\Lambda, \mathbb{R}) \to C(\Lambda, \mathbb{R})$, that reformulates problem (1) as a fixed-point problem, given by

$$\begin{aligned}\mathrm{Xu}(\bar{\boldsymbol{x}}, \tau) &= \mathrm{u}_0 + \frac{1-\sigma}{\mathrm{B}(\sigma)}\Big(a_1\Delta\mathrm{u}(\bar{\boldsymbol{x}}, \tau) - a_2\nabla\mathrm{u}(\bar{\boldsymbol{x}}, \tau) + \xi(\bar{\boldsymbol{x}}, \tau)\Big) \\ &\quad + \frac{\sigma}{\Gamma(\sigma)\mathrm{B}(\sigma)}\int_0^\tau (\tau - s)^{\sigma-1}\Big(a_1\Delta\mathrm{u}(\bar{\boldsymbol{x}}, \tau) - a_2\nabla\mathrm{u}(\bar{\boldsymbol{x}}, \tau) + \xi(\bar{\boldsymbol{x}}, \tau)\Big)ds.\end{aligned} \tag{5}$$

The fixed point of X, corresponds to the solution of problem (1). We assume the following hypotheses before proving our main results: for any $(\bar{\boldsymbol{x}}, \tau) \in \Lambda$, there exist $\kappa_k > 0$, $k = 1,2,3,4,5,6$, such that

$(\mathbf{A_1})$ $|\Delta\mathrm{u}(\bar{\boldsymbol{x}}, \tau)| \le \kappa_1|\mathrm{u}(\bar{\boldsymbol{x}}, \tau)|$,
$(\mathbf{A_2})$ $|\nabla\mathrm{u}(\bar{\boldsymbol{x}}, \tau)| \le \kappa_2|\mathrm{u}(\bar{\boldsymbol{x}}, \tau)|$,
$(\mathbf{A_3})$ $|\mathrm{u}_0| \le \kappa_3$,
$(\mathbf{A_4})$ $|\xi(\bar{\boldsymbol{x}}, \tau)| \le \kappa_4$,
$(\mathbf{A_5})$ $|\Delta\mathrm{u}_1(\bar{\boldsymbol{x}}, \tau) - \Delta\mathrm{u}_2(\bar{\boldsymbol{x}}, \tau)| \le \kappa_5|\mathrm{u}_1(\bar{\boldsymbol{x}}, \tau) - \mathrm{u}_2(\bar{\boldsymbol{x}}, \tau)|$,
$(\mathbf{A_6})$ $|\nabla\mathrm{u}_1(\bar{\boldsymbol{x}}, \tau) - \nabla\mathrm{u}_2(\bar{\boldsymbol{x}}, \tau)| \le \kappa_6|\mathrm{u}_1(\bar{\boldsymbol{x}}, \tau) - \mathrm{u}_2(\bar{\boldsymbol{x}}, \tau)|$.

Theorem 1. *If assumptions* $(\mathbf{A_5}, \mathbf{A_6})$ *hold then problem (1) has a unique solution.*

Proof. The proof consists of several steps.

Step 1: Continuity of X. We will show that X is continuous. Suppose a sequence $\mathrm{u}_m \to \mathrm{u}$, where $\mathrm{u} \in C(\Lambda, \mathbb{R})$. For $(\bar{\boldsymbol{x}}, \tau) \in \Lambda$ and using the bounds in $(\mathbf{A_5}, \mathbf{A_6})$ we can write

$$
\begin{aligned}
&\|\mathrm{Xu}_m(\bar{\boldsymbol{x}}, \tau) - \mathrm{Xu}(\bar{\boldsymbol{x}}, \tau)\|_\infty = \sup\left\{|\mathrm{Xu}_m(\bar{\boldsymbol{x}}, \tau) - \mathrm{Xu}(\bar{\boldsymbol{x}}, \tau)|\right\} \\
&= \sup\left\{\left|\frac{1-\sigma}{\mathrm{B}(\sigma)}\left(a_1\Delta\mathrm{u}_m(\bar{\boldsymbol{x}}, \tau) - a_2\nabla\mathrm{u}_m(\bar{\boldsymbol{x}}, \tau)\right) + \frac{\sigma}{\Gamma(\sigma)\mathrm{B}(\sigma)}\int_0^\tau(\tau-s)^{\sigma-1}\left(a_1\Delta\mathrm{u}_m(\bar{\boldsymbol{x}}, \tau) - a_2\nabla\mathrm{u}_m(\bar{\boldsymbol{x}}, \tau)\right)ds\right.\right. \\
&\quad \left.\left. - \frac{1-\sigma}{\mathrm{B}(\sigma)}\left(a_1\Delta\mathrm{u}(\bar{\boldsymbol{x}}, \tau) - a_2\nabla\mathrm{u}(\bar{\boldsymbol{x}}, \tau)\right) - \frac{\sigma}{\Gamma(\sigma)\mathrm{B}(\sigma)}\int_0^\tau(\tau-s)^{\sigma-1}\left(a_1\Delta\mathrm{u}(\bar{\boldsymbol{x}}, \tau) - a_2\nabla\mathrm{u}(\bar{\boldsymbol{x}}, \tau)\right)ds\right|\right\} \\
&\le \sup\left\{\frac{1-\sigma}{\mathrm{B}(\sigma)}\left(|a_1||\Delta\mathrm{u}_m(\bar{\boldsymbol{x}}, \tau) - \Delta\mathrm{u}(\bar{\boldsymbol{x}}, \tau)| + |a_2||\nabla\mathrm{u}_m(\bar{\boldsymbol{x}}, \tau) - \nabla\mathrm{u}(\bar{\boldsymbol{x}}, \tau)|\right)\right. \\
&\quad \left. - \frac{\sigma}{\Gamma(\sigma)\mathrm{B}(\sigma)}\int_0^\tau(\tau-s)^{\sigma-1}\left(|a_1||\Delta\mathrm{u}_m(\bar{\boldsymbol{x}}, \tau) - \Delta\mathrm{u}(\bar{\boldsymbol{x}}, \tau)| + |a_2||\nabla\mathrm{u}_m(\bar{\boldsymbol{x}}, \tau) - \nabla\mathrm{u}(\bar{\boldsymbol{x}}, \tau)|\right)ds\right\} \\
&\le \sup\left\{\frac{1-\sigma}{\mathrm{B}(\sigma)} + \frac{\sigma}{\Gamma(\sigma)\mathrm{B}(\sigma)}\int_0^\tau(\tau-s)^{\sigma-1}\left(\kappa_5|a_1||\mathrm{u}_m(\bar{\boldsymbol{x}}, \tau) - \mathrm{u}(\bar{\boldsymbol{x}}, \tau)| + \kappa_6|a_2||\mathrm{u}_m(\bar{\boldsymbol{x}}, \tau) - \mathrm{u}(\bar{\boldsymbol{x}}, \tau)|\right)ds\right\} \\
&\le \sup\left\{\frac{1-\sigma}{\mathrm{B}(\sigma)} + \frac{\tau^\sigma}{\Gamma(\sigma)\mathrm{B}(\sigma)}\left(\kappa_5|a_1| + \kappa_6|a_2|\right)|\mathrm{u}_m(\bar{\boldsymbol{x}}, \tau) - \mathrm{u}(\bar{\boldsymbol{x}}, \tau)|\right\} \\
&\le \frac{\tau^\sigma + (1-\sigma)\Gamma(\sigma)}{\Gamma(\sigma)\mathrm{B}(\sigma)}\left(\kappa_5|a_1| + \kappa_6|a_2|\right)\|\mathrm{u}_m - \mathrm{u}\|_\infty,
\end{aligned}
$$

Since u is continuous. Hence, we obtain

$$\|\mathrm{u}_m - \mathrm{u}\|_\infty \to 0, \text{ as } m \to \infty.$$

Therefore, X is continuous.

Step 2: Boundedness of X. Next, we show that X maps bounded sets to bounded sets. It is sufficient to prove that for $\gamma > 0$ there exists $\rho > 0$ such that if $\mathrm{u} \in R_\gamma = \{\mathrm{u} \in C(\Lambda, \mathbb{R}) : \|\mathrm{u}\|_\infty \le \gamma\}$ then it is $\|\mathrm{Xu}\|_\infty \le \rho$. For $\tau \in [0, T]$ and utilizing the assumptions $(\mathbf{A}_1\text{–}\mathbf{A}_4)$ we have

$$
\begin{aligned}
|\mathrm{Xu}(\bar{\boldsymbol{x}}, \tau)| &= \left|\mathrm{u}_0 + \frac{1-\sigma}{\mathrm{B}(\sigma)}\left(a_1\Delta\mathrm{u}(\bar{\boldsymbol{x}}, \tau) - a_2\nabla\mathrm{u}(\bar{\boldsymbol{x}}, \tau) + \xi(\bar{\boldsymbol{x}}, \tau)\right) + \frac{\sigma}{\Gamma(\sigma)\mathrm{B}(\sigma)}\int_0^\tau(\tau-s)^{\sigma-1}\left(a_1\Delta\mathrm{u}(\bar{\boldsymbol{x}}, \tau)\right.\right. \\
&\quad \left.\left. - a_2\nabla\mathrm{u}(\bar{\boldsymbol{x}}, \tau) + \xi(\bar{\boldsymbol{x}}, \tau)\right)ds\right| \\
&\le |\mathrm{u}_0| + \frac{1-\sigma}{\mathrm{B}(\sigma)}\left(|a_1||\Delta\mathrm{u}(\bar{\boldsymbol{x}}, \tau)| + |a_2||\nabla\mathrm{u}(\bar{\boldsymbol{x}}, \tau)| + |\xi(\bar{\boldsymbol{x}}, \tau)|\right) + \frac{\sigma}{\Gamma(\sigma)\mathrm{B}(\sigma)}\int_0^\tau(\tau-s)^{\sigma-1} \\
&\quad \left(|a_1||\Delta\mathrm{u}(\bar{\boldsymbol{x}}, \tau)| + |a_2||\nabla\mathrm{u}(\bar{\boldsymbol{x}}, \tau)| + |\xi(\bar{\boldsymbol{x}}, \tau)|\right)ds \\
&\le \kappa_3 + \frac{1-\sigma}{\mathrm{B}(\sigma)}\left(\kappa_1|a_1||\mathrm{u}(\bar{\boldsymbol{x}}, \tau)| + \kappa_2|a_2||\mathrm{u}(\bar{\boldsymbol{x}}, \tau)| + \kappa_4\right) + \frac{\sigma}{\Gamma(\sigma)\mathrm{B}(\sigma)}\int_0^\tau(\tau-s)^{\sigma-1}\left(\kappa_1|a_1||\mathrm{u}(\bar{\boldsymbol{x}}, \tau)|\right. \\
&\quad \left. + \kappa_2|a_2||\mathrm{u}(\bar{\boldsymbol{x}}, \tau)| + \kappa_4\right)ds
\end{aligned}
$$

$$\leq \kappa_3 + \frac{1-\sigma}{\mathrm{B}(\sigma)}\left(|a_1|\kappa_1\|\mathrm{u}\|_\infty + |a_2|\kappa_2\|\mathrm{u}\|_\infty + \kappa_4\right) + \frac{\sigma}{\Gamma(\sigma)\mathrm{B}(\sigma)}\int_0^\tau (\tau - s)^{\sigma-1}$$
$$\left(|a_1|\kappa_1\|\mathrm{u}\|_\infty + |a_2|\kappa_2\|\mathrm{u}\|_\infty + \kappa_4\right)ds$$
$$\leq \kappa_3 + \frac{(1-\sigma)\Gamma(\sigma)}{\mathrm{B}(\sigma)}\left(|a_1|\kappa_1\|\mathrm{u}\|_\infty + |a_2|\kappa_2\|\mathrm{u}\|_\infty + \kappa_4\right) + \frac{\tau^\sigma}{\Gamma(\sigma)\mathrm{B}(\sigma)}\left(\kappa_1|a_1|\|\mathrm{u}\|_\infty + |a_2|\kappa_2\|\mathrm{u}\|_\infty + \kappa_4\right)$$
$$\leq \kappa_3 + \frac{(1-\sigma)\Gamma(\sigma) + \tau^\sigma}{\Gamma(\sigma)\mathrm{B}(\sigma)}\left(\kappa_1|a_1|\|\mathrm{u}\|_\infty + \kappa_2|a_2|\|\mathrm{u}\|_\infty + \kappa_4\right)$$
$$\leq \kappa_3 + \frac{(1-\sigma)\Gamma(\sigma) + \tau^\sigma}{\Gamma(\sigma)\mathrm{B}(\sigma)}\left(\left(\kappa_1|a_1| + \kappa_2|a_2|\right)\|\mathrm{u}\|_\infty + \kappa_4\right).$$

Defining

$$\rho = \kappa_3 + \frac{\tau^\sigma + \Gamma(\sigma)(1-\sigma)}{\Gamma(\sigma)\mathrm{B}(\sigma)}\left(\left(\kappa_1|a_1| + \kappa_2|a_2|\right)\gamma + \kappa_4\right),$$

it follows that $\|\mathrm{Xu}\|_\infty \leq \rho$ proving that X maps bounded sets to bounded sets.

Step 3: Equicontinuity of X. Let consider $\mathrm{u} \in R_\gamma$ and $(\bar{\boldsymbol{x}}_1, \tau_1), (\bar{\boldsymbol{x}}_2, \tau_2) \in \Lambda$, such that $\bar{\boldsymbol{x}}_1 < \bar{\boldsymbol{x}}_2,\ \tau_1 < \tau_2$. We have

$$|\mathrm{Xu}(\bar{\boldsymbol{x}}_1, \tau_1) - \mathrm{Xu}(\bar{\boldsymbol{x}}_2, \tau_2)| = \left|\frac{1-\sigma}{\mathrm{B}(\sigma)}\left(a_1\Delta\mathrm{u}(\bar{\boldsymbol{x}}_1, \tau_1) - a_2\nabla\mathrm{u}(\bar{\boldsymbol{x}}_1, \tau_1) + \xi(\bar{\boldsymbol{x}}_1, \tau_1)\right)\right.$$
$$+ \frac{\sigma}{\Gamma(\sigma)\mathrm{B}(\sigma)}\int_0^{\tau_1}(\tau_1 - s_1)^{\sigma-1}\left(a_1\Delta\mathrm{u}(\bar{\boldsymbol{x}}_1, \tau_1) - a_2\nabla\mathrm{u}(\bar{\boldsymbol{x}}_1, \tau_1) + \xi(\bar{\boldsymbol{x}}_1, \tau_1)\right)ds_1$$
$$- \frac{1-\sigma}{\mathrm{B}(\sigma)}\left(a_1\Delta\mathrm{u}(\bar{\boldsymbol{x}}_2, \tau_2) - a_2\nabla\mathrm{u}(\bar{\boldsymbol{x}}_2, \tau_2)\right) - \frac{\sigma}{\Gamma(\sigma)\mathrm{B}(\sigma)}\int_0^{\tau_2}(\tau_2 - s_2)^{\sigma-1}$$
$$\left.\left(a_1\Delta\mathrm{u}(\bar{\boldsymbol{x}}_2, \tau_2) - a_2\nabla\mathrm{u}(\bar{\boldsymbol{x}}_2, \tau_2) + \xi(\bar{\boldsymbol{x}}_2, \tau_2)\right)ds_2\right|$$
$$\leq \frac{1-\sigma}{\mathrm{B}(\sigma)}\left(|a_1||\Delta\mathrm{u}(\bar{\boldsymbol{x}}_1, \tau_1)| + |a_2||\nabla\mathrm{u}(\bar{\boldsymbol{x}}_1, \tau_1)| + |\xi(\bar{\boldsymbol{x}}_1, \tau_1)|\right)$$
$$+ \frac{\sigma}{\Gamma(\sigma)\mathrm{B}(\sigma)}\int_0^{\tau_1}(\tau_1 - s_1)^{\sigma-1}\left(|a_1||\Delta\mathrm{u}(\bar{\boldsymbol{x}}_1, \tau_1)| + |a_2||\nabla\mathrm{u}(\bar{\boldsymbol{x}}_1, \tau_1)| + |\xi(\bar{\boldsymbol{x}}_1, \tau_1)|\right)ds_1$$
$$- \frac{1-\sigma}{\mathrm{B}(\sigma)}\left(|a_1||\Delta\mathrm{u}(\bar{\boldsymbol{x}}_2, \tau_2)| + |a_2||\nabla\mathrm{u}(\bar{\boldsymbol{x}}_2, \tau_2)| + |\xi(\bar{\boldsymbol{x}}_2, \tau_2)|\right)$$
$$- \frac{\sigma}{\Gamma(\sigma)\mathrm{B}(\sigma)}\int_0^{\tau_2}(\tau_2 - s_2)^{\sigma-1}\left(|a_1||\Delta\mathrm{u}(\bar{\boldsymbol{x}}_2, \tau_2)| + |a_2||\nabla\mathrm{u}(\bar{\boldsymbol{x}}_2, \tau_2)| + |\xi(\bar{\boldsymbol{x}}_2, \tau_2)|\right)ds_2$$
$$\leq \frac{1-\sigma}{\mathrm{B}(\sigma)}\left(\kappa_1|a_1||\mathrm{u}(\bar{\boldsymbol{x}}_1, \tau_1)| + \kappa_2|a_2||\mathrm{u}(\bar{\boldsymbol{x}}_1, \tau_1)| + \kappa_4\right)$$
$$+ \frac{\sigma}{\Gamma(\sigma)\mathrm{B}(\sigma)}\int_0^{\tau_1}(\tau_1 - s_1)^{\sigma-1}\left(|a_1|\kappa_1|\mathrm{u}(\bar{\boldsymbol{x}}_1, \tau_1)| + |a_2|\kappa_2|\mathrm{u}(\bar{\boldsymbol{x}}_1, \tau_1)| + \kappa_4\right)ds_1$$
$$- \frac{1-\sigma}{\mathrm{B}(\sigma)}\left\{|a_1|\kappa_1|\mathrm{u}(\bar{\boldsymbol{x}}_2, \tau_2)| + |a_2|\kappa_2|\mathrm{u}(\bar{\boldsymbol{x}}_2, \tau_2)| + \kappa_4\right\}$$

$$
\begin{aligned}
&- \frac{\sigma}{\Gamma(\sigma)\mathrm{B}(\sigma)} \int_0^{\tau_1} (\tau_2 - s_2)^{\sigma-1} \Big(|a_1|\kappa_1|\mathrm{u}(\bar{\boldsymbol{x}}_2, \tau_2)| + |a_2|\kappa_2|\mathrm{u}(\bar{\boldsymbol{x}}_2, \tau_2)| + \kappa_4 \Big) ds_2 \\
&\leq \frac{1-\sigma}{\mathrm{B}(\sigma)} \Big(|a_1|\kappa_1\|\mathrm{u}\|_\infty + |a_2|\kappa_2\|\mathrm{u}\|_\infty + \kappa_4 \Big) + \frac{\sigma}{\Gamma(\sigma)\mathrm{B}(\sigma)} \int_0^{\tau_1} (\tau_1 - s_1)^{\sigma-1} \Big(|a_1|\kappa_1\|\mathrm{u}\|_\infty + |a_2|\kappa_2\|\mathrm{u}\|_\infty + \kappa_4 \Big) ds_1 \\
&- \frac{1-\sigma}{\mathrm{B}(\sigma)} \Big(|a_1|\kappa_1\|\mathrm{u}\|_\infty + |a_2|\kappa_2\|\mathrm{u}\|_\infty + \kappa_4 \Big) - \frac{\sigma}{\Gamma(\sigma)\mathrm{B}(\sigma)} \int_0^{\tau_2} (\tau_2 - s_2)^{\sigma-1} \Big(|a_1|\kappa_1\|\mathrm{u}\|_\infty + |a_2|\kappa_2\|\mathrm{u}\|_\infty + \kappa_4 \Big) ds_2 \\
&= \frac{\sigma}{\Gamma(\sigma)\mathrm{B}(\sigma)} \int_0^{\tau_1} (\tau_1 - s_1)^{\sigma-1} \Big(|a_1|\kappa_1\|\mathrm{u}\|_\infty + |a_2|\kappa_2\|\mathrm{u}\|_\infty + \kappa_4 \Big) ds_1 \\
&- \frac{\sigma}{\Gamma(\sigma)\mathrm{B}(\sigma)} \int_0^{\tau_2} (\tau_2 - s_2)^{\sigma-1} \Big(|a_1|\kappa_1\|\mathrm{u}\|_\infty + |a_2|\kappa_2\|\mathrm{u}\|_\infty + \kappa_4 \Big) ds_2 \\
&= \left(\int_0^{\tau_1} (\tau_1 - s_1)^{\sigma-1} ds_1 - \int_0^{\tau_2} (\tau_2 - s_2)^{\sigma-1} ds_2 \right) \left[\frac{\sigma}{\Gamma(\sigma)\mathrm{B}(\sigma)} \Big(|a_1|\kappa_1\|\mathrm{u}\|_\infty + |a_2|\kappa_2\|\mathrm{u}\|_\infty + \kappa_4 \Big) \right] \\
&= \frac{\tau_1^\sigma - \tau_2^\sigma}{\Gamma(\sigma)\mathrm{B}(\sigma)} \Big(|a_1|\kappa_1\|\mathrm{u}\|_\infty + |a_2|\kappa_2\|\mathrm{u}\|_\infty + \kappa_4 \Big).
\end{aligned}
$$

It follows that

$$|\mathrm{Xu}(\bar{\boldsymbol{x}}_1, \tau_1) - \mathrm{Xu}(\bar{\boldsymbol{x}}_2, \tau_2)| \to 0 \quad \text{as } \tau_1 \to \tau_2.$$

By the Arzelà-Ascoli Theorem [61], the operator X is completely continuous.

Step 4: A Priori Bound. Define $\chi = \{\mathrm{u} \in C(\Lambda, \mathbb{R}) : \mathrm{u} = \varepsilon \mathrm{Xu}, \varepsilon \in (0,1)\}$. We prove that χ is bounded. If $\mathrm{u} \in \chi$, then $\mathrm{u} = \varepsilon \mathrm{Xu}$, with $0 < \varepsilon < 1$. Then for $\tau \in [0, T]$, using Eq. (5) we have

$$
\begin{aligned}
|\mathrm{u}| &= |\varepsilon \mathrm{Xu}| \\
&= \left| \varepsilon \times \left(\mathrm{u}_0 + \frac{1-\sigma}{\mathrm{B}(\sigma)} \Big(a_1 \Delta \mathrm{u}(\bar{\boldsymbol{x}}, \tau) - a_2 \nabla \mathrm{u}(\bar{\boldsymbol{x}}, \tau) + \xi(\bar{\boldsymbol{x}}, \tau) \Big) + \frac{\sigma}{\Gamma(\sigma)\mathrm{B}(\sigma)} \int_0^{\tau} (\tau - s)^{\sigma-1} \Big(a_1 \Delta \mathrm{u}(\bar{\boldsymbol{x}}, \tau) \right. \right. \\
&\quad \left. \left. - a_2 \nabla \mathrm{u}(\bar{\boldsymbol{x}}, \tau) + \xi(\bar{\boldsymbol{x}}, \tau) \Big) ds \right) \right|.
\end{aligned}
$$

Now, using assumptions $(\mathbf{A_1} - \mathbf{A_4})$ we get

$$|\mathrm{u}| = \varepsilon \times \left(\kappa_3 + \frac{(1-\sigma)\Gamma(\sigma) + \tau^\sigma}{\Gamma(\sigma)\mathrm{B}(\sigma)} \Big(\big(\kappa_1|a_1| + \kappa_2|a_2| \big) \|\mathrm{u}\|_\infty + \kappa_4 \Big) \right),$$

which gives

$$\|\mathrm{u}\|_\infty = \varepsilon \times \rho,$$

where ρ is as defined in Step 2. This shows that χ is bounded. By the Schaefer Fixed Point Theorem [61], X has at least one fixed point. Consequently, the considered problem has at least one solution. □ (25A1)

Theorem 2. *The problem define in Eq. (1) has a unique solution if the assumptions* $(\mathbf{A_5}, \mathbf{A_6})$ *hold and*

$$\frac{(1-\sigma)\Gamma(\sigma) + \tau^\sigma}{\Gamma(\sigma)\mathrm{B}(\sigma)} \Big\{ \kappa_5|a_1| + \kappa_6|a_2| \Big\} < 1.$$

Proof

$$\begin{aligned}
&\|\mathrm{Xu}_1(\bar{\boldsymbol{x}},\tau)-\mathrm{Xu}_2(\bar{\boldsymbol{x}},\tau)\|_\infty = \sup\left\{|\mathrm{Xu}_1(\bar{\boldsymbol{x}},\tau)-\mathrm{Xu}_2(\bar{\boldsymbol{x}},\tau)|\right\}\\
&= \sup\left\{\left|\frac{1-\sigma}{\mathrm{B}(\sigma)}\Big(a_1\Delta\mathrm{u}_1(\bar{\boldsymbol{x}},\tau)-a_2\nabla\mathrm{u}_1(\bar{\boldsymbol{x}},\tau)\Big)+\frac{\sigma}{\Gamma(\sigma)\mathrm{B}(\sigma)}\int_0^\tau(\tau-s)^{\sigma-1}\Big(a_1\Delta\mathrm{u}_1(\bar{\boldsymbol{x}},\tau)-a_2\nabla\mathrm{u}_1(\bar{\boldsymbol{x}},\tau)\Big)ds\right.\\
&\left.-\frac{1-\sigma}{\mathrm{B}(\sigma)}\Big(a_1\Delta\mathrm{u}_2(\bar{\boldsymbol{x}},\tau)-a_2\nabla\mathrm{u}_2(\bar{\boldsymbol{x}},\tau)\Big)-\frac{\sigma}{\Gamma(\sigma)\mathrm{B}(\sigma)}\int_0^\tau(\tau-s)^{\sigma-1}\Big(a_1\Delta\mathrm{u}_2(\bar{\boldsymbol{x}},\tau)-a_2\nabla\mathrm{u}_2(\bar{\boldsymbol{x}},\tau)\Big)ds\right|\Bigg\}\\
&\le \sup\left\{\frac{1-\sigma}{\mathrm{B}(\sigma)}\Big(|a_1||\Delta\mathrm{u}_1(\bar{\boldsymbol{x}},\tau)-\Delta\mathrm{u}_2(\bar{\boldsymbol{x}},\tau)|+|a_2||\nabla\mathrm{u}_1(\bar{\boldsymbol{x}},\tau)-\nabla\mathrm{u}_2(\bar{\boldsymbol{x}},\tau)|\Big)\right.\\
&\left.-\frac{\sigma}{\Gamma(\sigma)\mathrm{B}(\sigma)}\int_0^\tau(\tau-s)^{\sigma-1}\Big(|a_1||\Delta\mathrm{u}_1(\bar{\boldsymbol{x}},\tau)-\Delta\mathrm{u}_2(\bar{\boldsymbol{x}},\tau)|+|a_2||\nabla\mathrm{u}_1(\bar{\boldsymbol{x}},\tau)-\nabla\mathrm{u}_2(\bar{\boldsymbol{x}},\tau)|\Big)ds\right\}\\
&\le \sup\left\{\frac{1-\sigma}{\mathrm{B}(\sigma)}+\frac{\sigma}{\Gamma(\sigma)\mathrm{B}(\sigma)}\int_0^\tau(\tau-s)^{\sigma-1}\Big(\kappa_5|a_1||\mathrm{u}_1(\bar{\boldsymbol{x}},\tau)-\mathrm{u}_2(\bar{\boldsymbol{x}},\tau)|+\kappa_6|a_2||\mathrm{u}_1(\bar{\boldsymbol{x}},\tau)-\mathrm{u}_2(\bar{\boldsymbol{x}},\tau)|\Big)ds\right\}\\
&\le \sup\left\{\frac{1-\sigma}{\mathrm{B}(\sigma)}+\frac{\tau^\sigma}{\Gamma(\sigma)\mathrm{B}(\sigma)}\Big(\kappa_5|a_1|+\kappa_6|a_2|\Big)|\mathrm{u}_1(\bar{\boldsymbol{x}},\tau)-\mathrm{u}_2(\bar{\boldsymbol{x}},\tau)|\right\}\\
&\le \frac{\tau^\sigma+(1-\sigma)\Gamma(\sigma)}{\Gamma(\sigma)\mathrm{B}(\sigma)}\Big(\kappa_5|a_1|+\kappa_6|a_2|\Big)\|\mathrm{u}_1-\mathrm{u}_2\|_\infty.
\end{aligned}$$

Thus, we find that under the given assumptions X is a contraction. By the Banach Fixed-Point Theorem [61], X has a unique fixed point. Therefore, the problem defined in Eq. (1) has a unique solution. □ (25A1)

3 Methodology

In the LT-CSCM approach, the Laplace Transform (LT) transforms Eq. (1) into the Laplace domain, enabling efficient temporal discretization. The Chebyshev Spectral Collocation Method (CSCM) is then applied to discretize spatial variables with high accuracy. Finally, the time-domain solution is recovered using the Talbot method for numerical inverse Laplace transform, ensuring precision and computational efficiency.

3.1 Temporal Discretization

The Laplace Transform is used for the temporal discretization of the proposed problem defined in Eq. (1). The LT of $\mathrm{u}(\bar{\boldsymbol{x}},\tau)$ is defined as

$$\mathscr{L}\{\mathrm{u}(\bar{\boldsymbol{x}},\tau)\} = \widehat{\mathrm{u}}(\bar{\boldsymbol{x}},\mathrm{s}) = \int_0^\infty e^{-\mathrm{s}\tau}\mathrm{u}(\bar{\boldsymbol{x}},\tau)d\tau.$$

The LT of the ABC derivative, $\partial_\tau^\sigma \mathrm{u}(\bar{\boldsymbol{x}},\tau)$, defined in Eq. (2), is given by [8]

$$\mathscr{L}\{\partial_\tau^\sigma \mathrm{u}(\bar{\boldsymbol{x}},\tau)\} = \frac{\mathrm{B}(\sigma)\big(\mathrm{s}^\sigma\widehat{\mathrm{u}}(\bar{\boldsymbol{x}},\mathrm{s})-\mathrm{s}^{\sigma-1}\mathrm{u}_0\big)}{\mathrm{s}^\sigma(1-\sigma)+\sigma}.$$

Applying the LT to Eq. (1) yields

$$\frac{\mathrm{B}(\sigma)\big(\mathrm{s}^\sigma\widehat{\mathrm{u}}(\bar{\boldsymbol{x}},\mathrm{s})-\mathrm{s}^{\sigma-1}\mathrm{u}_0\big)}{\mathrm{s}^\sigma(1-\sigma)+\sigma} = \mathfrak{L}\widehat{\mathrm{u}}(\bar{\boldsymbol{x}},\mathrm{s})+\widehat{\xi}(\bar{\boldsymbol{x}},\mathrm{s}),\quad \bar{\boldsymbol{x}}\in\Theta, \tag{6}$$

and

$$\mathfrak{B}\widehat{\mathrm{u}}(\bar{\boldsymbol{x}},\mathrm{s}) = \widehat{\zeta}(\bar{\boldsymbol{x}},\mathrm{s}), \quad \bar{\boldsymbol{x}} \in \partial\Theta. \tag{7}$$

Simplifying further, we obtain

$$\left\{\left(\frac{\mathrm{B}(\sigma)\mathrm{s}^{\sigma}}{\mathrm{s}^{\sigma}(1-\sigma)+\sigma}\right)I - \mathfrak{L}\right\}\widehat{\mathrm{u}}(\bar{\boldsymbol{x}},\mathrm{s}) = \widehat{\mathrm{S}}(\bar{\boldsymbol{x}},\mathrm{s}), \quad \bar{\boldsymbol{x}} \in \Theta, \tag{8}$$

and

$$\mathfrak{B}\widehat{\mathrm{u}}(\bar{\boldsymbol{x}},\mathrm{s}) = \widehat{\zeta}(\bar{\boldsymbol{x}},\mathrm{s}), \quad \bar{\boldsymbol{x}} \in \partial\Theta, \tag{9}$$

where

$$\widehat{\mathrm{S}}(\bar{\boldsymbol{x}},\mathrm{s}) = \frac{\mathrm{B}(\sigma)\mathrm{s}^{\sigma-1}\mathrm{u}_0}{\mathrm{s}^{\sigma}(1-\sigma)+\sigma} + \widehat{\xi}(\bar{\boldsymbol{x}},\mathrm{s}),$$

and I is the $(\mathrm{N}+1)\times(\mathrm{N}+1)$ identity operator. The time independent problem in Eqs. (8) and (9) is solved for each s in the Laplace space, using CSCM for spatial discretization. Finally, numerical ILTM is used to to recover the time-domain solution of (1). The next section explains the CSCM approach.

3.2 Spatial Discretization by Chebyshev Spectral Collocation Method

In CSCM, a global polynomial interpolant is utilized on specific nodes (Chebychev nodes) to approximate the unknown solution of a FPDEs. The spatial derivatives are computed using discrete derivative operators, also called differentiation matrices (DM) [41].

The solution is considered over $[-1,1]$ and interpolates $\{(x_{\mathrm{m}},\widehat{\mathrm{u}}(x_{\mathrm{m}}))\}$, by [42,46]

$$\mathbf{I}_{\mathrm{N}}(x) = \sum_{\mathrm{m}=0}^{\mathrm{N}} l_{\mathrm{m}}(x)\widehat{\mathrm{u}}_{\mathrm{m}},$$

where $\widehat{\mathrm{u}}_{\mathrm{m}} = \widehat{\mathrm{u}}(x_{\mathrm{m}})$, and the basic Lagrange polynomials are as follows:

$$l_{\mathrm{m}}(x) = \frac{(x-x_0)\ldots(x-x_{\mathrm{m}-1})(x-x_{\mathrm{m}+1})\ldots(x-x_{\mathrm{N}})}{(x_{\mathrm{m}}-x_0)\ldots(x_{\mathrm{m}}-x_{\mathrm{m}-1})(x_{\mathrm{m}}-x_{\mathrm{m}+1})\ldots(x_{\mathrm{m}}-x_{\mathrm{N}})}. \tag{10}$$

For spatial discretization in $[-1,1]$, the Chebyshev nodes are usually considered

$$x_{\mathrm{m}} = \cos\left\{\left(\frac{l\pi}{\mathrm{N}}\right)\right\}_{\mathrm{m}=0}^{\mathrm{N}}. \tag{11}$$

The first derivative $\widehat{\mathrm{u}}_x$ is approximated as

$$\partial_x\widehat{\mathrm{u}}(x) \approx \mathrm{D}_{\mathrm{N}}\widehat{\mathrm{u}},$$

where D_{N} is the first-order differentiation matrix with entries of the form

$$[\mathrm{D}_{\mathrm{N}}]_{\mathrm{n,m}} = \left\{l'_{\mathrm{m}}(x_{\mathrm{n}})\right\}_{\mathrm{n,m}=1}^{\mathrm{N}}.$$

The non-diagonal entries of $\mathrm{D_N}$ are given as

$$[\mathrm{D_N}]_{\mathrm{n,m}} = \frac{\gamma_{\mathrm{m}}}{\gamma_{\mathrm{n}}(x_{\mathrm{n}} - x_{\mathrm{m}})}, \mathrm{n} \neq \mathrm{m},$$

where $\gamma_{\mathrm{m}}^{-1} = \prod_{\mathrm{n}\neq\mathrm{m}}^{n}(x_{\mathrm{n}} - x_{\mathrm{m}})$, and the diagonal entries of $\mathrm{D_N}$ are calculated by

$$[\mathrm{D_N}]_{\mathrm{n,m}} = -\sum_{\mathrm{m}=0,\mathrm{m}\neq\mathrm{n}}^{n}\{\mathrm{D_N}\}_{\mathrm{n,m}}, \quad \mathrm{n,m} \in \{0,1,2,\ldots,\mathrm{N}\}.$$

The elements of the DM, $\mathrm{D_N}$ of order ρ are analytically calculated as

$$[\mathrm{D_N^{\rho}}]_{\mathrm{n,m}} = \left\{ l_{\mathrm{m}}^{\rho}(x_{\mathrm{n}}) \right\}_{\mathrm{n,m}=1}^{\mathrm{N}}.$$

More efficient elaboration of the differentiation matrices can be found in [62]. Welfert [41], obtained an easy to use recursion relation for the calculation of differentiation matrix, as follows:

$$[\mathrm{D_N^{\rho}}]_{\mathrm{n,m}} = \frac{\rho}{x_{\mathrm{n}} - x_{\mathrm{m}}}\left\{ \frac{\gamma_{\mathrm{m}}}{\gamma_{\mathrm{n}}}[\mathrm{D_N^{(\rho-1)}}]_{\mathrm{nn}} - [\mathrm{D_N^{(\rho-1)}}]_{\mathrm{nm}} \right\}, \ \mathrm{n} \neq \mathrm{m}.$$

For the square domain $\Theta = [-1,1] \times [-1,1]$, the Chebyshev nodes are $\boldsymbol{x}_{\mathrm{nm}}$, and is presented as

$$\bar{\boldsymbol{x}}_{\mathrm{nm}} = \left\{ \left(\cos\left(\frac{\mathrm{n}\pi}{\mathrm{N}}\right), \cos\left(\frac{\mathrm{m}\pi}{\mathrm{N}}\right) \right) \right\}_{\mathrm{n,m}=1}^{\mathrm{N}}.$$

The basic Lagrange polynomials associated to $\boldsymbol{v}_{\mathrm{nm}}$ are written as

$$l_{\mathrm{nm}}(\bar{\boldsymbol{x}}) = l_{\mathrm{n}}(x) l_{\mathrm{m}}(y), \tag{12}$$

with $l_{\mathrm{nm}}(\bar{\boldsymbol{x}}_{\mathrm{nm}}) = [\phi_{\mathrm{nm}}]_{\mathrm{n,m}=0}^{\mathrm{N}}$, and the second-order derivatives are calculated as

$$\partial_{xx}^2 l_{\mathrm{nm}}(\boldsymbol{x}_{rs}) = l_{\mathrm{n}}''(x_r) l_{\mathrm{m}}(y_s) = [\mathrm{D_N^2}]_{rn}\phi_{\mathrm{m}s},$$
$$\partial_{yy}^2 l_{\mathrm{nm}}(\boldsymbol{x}_{rs}) = l_{\mathrm{n}}(x_r) l_{\mathrm{m}}''(y_s) = \phi_{rn}[\mathrm{D_N^2}]_{sm},$$

where $\mathrm{D_N^2}$ is a differential matrix of 2^{nd} order based on collocation nodes. Applying the operator $\mathfrak{L}$ on Eq. (12) with collocation nodes $\boldsymbol{v}_{rs}$, we have

$$\mathfrak{L}(l_{\mathrm{nm}}(\boldsymbol{x}_{rs})) = a_1\left([\mathrm{D_N^2}]_{rn}\phi_{\mathrm{m}s} + \phi_{rn}[\mathrm{D_N^2}]_{sm} \right) - a_2\left([\mathrm{D_N}]_{rn}\phi_{\mathrm{m}s} + \phi_{rn}[\mathrm{D_N}]_{sm} \right). \tag{13}$$

Finally, the approximation of $\mathfrak{L}$ by the CSCM is given as

$$\mathfrak{L}_{Discrete} = a_1\left(\mathrm{D_N^2} \otimes I_{\mathrm{N}} + I_{\mathrm{N}} \otimes \mathrm{D_N^2} \right) - a_2\left(\mathrm{D_N} \otimes I_{\mathrm{N}} + I_{\mathrm{N}} \otimes \mathrm{D_N} \right). \tag{14}$$

By using Eq. (14) in Eq. (8), we get

$$\left\{ \left(\frac{\mathrm{B}(\sigma)\mathrm{s}^{\sigma}}{\mathrm{s}^{\sigma}(1-\sigma) + \sigma} \right) I - \mathfrak{L}_{Discrete} \right\} \widehat{\mathrm{u}}(\bar{\boldsymbol{x}}, \mathrm{s}) = \widehat{\mathrm{S}}(\bar{\boldsymbol{x}}, \mathrm{s}). \tag{15}$$

In order to incorporate the boundary conditions in Eq. (9), we consider $\mathfrak{L}_{Discrete}$, and all collocation nodes $\boldsymbol{x}$. Moreover, the rows of $\mathfrak{L}_{Discrete}$, are replaced by the corresponding nodes at the boundary with the vectors whose magnitude is one and having unity in a position corresponding to the diagonal of $\mathfrak{L}_{Discrete}$. So, the boundary conditions $\mathfrak{B}\widehat{\mathrm{u}}(\bar{\boldsymbol{x}},\mathrm{s}) = \widehat{\zeta}(\bar{\boldsymbol{x}},\mathrm{s})$ in Eq. (9) will be executed straightaway [42]. After re-organizing all the corresponding columns and rows of $\mathfrak{L}_{Discrete}$, we get the matrix:

$$\mathfrak{L}_{\Theta} = \begin{bmatrix} H & Q \\ 0 & I \end{bmatrix},$$

where H is the square matrix of order $(\mathrm{N} - \mathrm{N}_{\mathfrak{B}}) \times (\mathrm{N} - \mathrm{N}_{\mathfrak{B}})$, I is square matrix of order $(\mathrm{N}_{\mathfrak{B}} \times \mathrm{N}_{\mathfrak{B}})$, being the number of nodes at the boundary $\mathrm{N}_{\mathfrak{B}}$. The solution of the system (8) and (9) is reached after solving the system

$$\mathfrak{L}_{\Theta}\widehat{\mathrm{u}}(\bar{\boldsymbol{x}},\mathrm{s}) = \begin{bmatrix} \widehat{\mathrm{S}}(\bar{\boldsymbol{x}},\mathrm{s}) \\ \widehat{\zeta}(\bar{\boldsymbol{x}},\mathrm{s}) \end{bmatrix},$$

where the values of interior-boundary points are accumulated via $\widehat{\mathrm{S}}(\bar{\boldsymbol{x}},\mathrm{s})$ and $\widehat{\zeta}(\bar{\boldsymbol{x}},\mathrm{s})$ correspondingly. Finally, we will utilize the ILTMs to get the approximate solution of problem (1).

Error Bound of CSCM

As $\mathbf{I}_{\mathrm{N}} : C(\Theta) \to \mathbb{P}_{\mathrm{N}}$, depend on the Chebyshev nodes in Eq. (11) and Lagrange polynomial in Eq. (10) as follows:

$$\mathbf{I}_{\mathrm{N}}(\mathrm{u}) = \sum_{\mathrm{m}=0}^{\mathrm{N}} \mathrm{u}(x_m) l_{\mathrm{m}}(x). \tag{16}$$

For the calculation of the error bound of CSCM, we utilze the work of Börm et al. [63]. Suppose for all $\mathrm{u} \in C[-1,1]$, $\exists\ \Pi_{\mathrm{N}} > 0$, a constant, satisfies the inequality

$$\|\mathbf{I}_{\mathrm{N}}(\mathrm{u})\|_{\infty} \leq \Pi_{\mathrm{N}} \|\mathrm{u}\|_{\infty}. \tag{17}$$

Furthermore, for all $\mathrm{u} \in \mathbb{P}_{\mathrm{N}}$

$$\mathbf{I}_{\mathrm{N}}(\mathrm{u}) = \mathrm{u}. \tag{18}$$

For interpolation based on Chebyshev points, we have

$$\Pi_{\mathrm{N}} = \frac{\log_e(\mathrm{N}+1)}{\frac{\pi}{2}} + 1 \leq (1+\mathrm{N}). \tag{19}$$

The stability constant get larger very sluggishly [63], the approximation bound is given as

$$\|\mathrm{u} - \mathbf{I}_{\mathrm{N}}(\mathrm{u})\|_{\infty} \leq \frac{2^{-\mathrm{N}}}{(\mathrm{N}+1)!} \|\mathrm{u}^{\mathrm{N}+1}\|_{\infty} \ \forall\ \mathrm{u} \in C^{\mathrm{N}+1}, \tag{20}$$

Theorem 3 [63]. *If the polynomial interpolation error bound in (17) and the approximation bound in (20) hold for all* $\mathrm{u} \in C^{\mathrm{N}+1}$, *with* $\kappa \in \{0, 1, 2, \ldots, \mathrm{N}\}$, *then*

$$\|\mathrm{u}^{(\kappa)} - \mathbf{I}_{\mathrm{N}}(\mathrm{u})^{(\kappa)}\|_{\infty} \leq \frac{2\Pi_{\mathrm{N}}^{(\kappa)} + 2}{(1 + \mathrm{N} - \kappa)!}\left(\frac{1}{2}\right)^{(1+\mathrm{N}-\kappa)} \|\mathrm{u}^{(\mathrm{N}+1)}\|_{\infty}, \tag{21}$$

where $\Pi_{\mathrm{N}}^{(\kappa)}$ is given by

$$\Pi_{\mathrm{N}}^{(\kappa)} = \frac{\Pi_{\mathrm{N}}}{\kappa!}\left(\frac{\mathrm{N}!}{(\mathrm{N} - \kappa)!}\right).$$

The error bound is formulated by utilizing the results in Eq. (20) and Eq. (21), for $1 - D$ case the linear differential operator in Eq. (1) is $\mathfrak{L} = a_1 \frac{\partial^2}{\partial x^2} - a_2 \frac{\partial}{\partial x}$,

$$\begin{aligned}
\mathfrak{E} &= \|(\partial_\tau^\sigma \mathrm{u} - \mathfrak{L}\mathrm{u}) - (\partial_\tau^\sigma \mathbf{I}_{\mathrm{N}}(\mathrm{u}) - \mathfrak{L}\mathbf{I}_{\mathrm{N}}(\mathrm{u}))\|_{\infty} \\
&= \|\partial_\tau^\sigma(\mathrm{u} - \mathbf{I}_{\mathrm{N}}(\mathrm{u})) - \mathfrak{L}(\mathrm{u} - \mathbf{I}_{\mathrm{N}}(\mathrm{u}))\|_{\infty} \\
&\leq \|\partial_\tau^\sigma(\mathrm{u} - \mathbf{I}_{\mathrm{N}}(\mathrm{u}))\|_{\infty} + \|\mathfrak{L}(\mathrm{u} - \mathbf{I}_{\mathrm{N}}(\mathrm{u}))\|_{\infty} \\
&\leq \|\partial_\tau^\sigma(\mathrm{u} - \mathbf{I}_{\mathrm{N}}(\mathrm{u}))\|_{\infty} + |a_1|\|\mathrm{u}_{vv} - \mathbf{I}_{\mathrm{N}}(\mathrm{u})_{vv}\|_{\infty} + |a_2|\|\mathrm{u}_v - \mathbf{I}_{\mathrm{N}}(\mathrm{u})_v\|_{\infty} \\
\mathfrak{E} &\leq \|\partial_\tau^\sigma(\mathrm{u} - \mathbf{I}_{\mathrm{N}}(\mathrm{u}))\|_{\infty} + |a_1|\frac{2(\Pi_{\mathrm{N}}^{(2)} + 1)}{(\mathrm{N} - 1)!}\left(\frac{1}{2}\right)^{\mathrm{N}-1} \|\mathrm{u}^{(1+\mathrm{N})}\|_{\infty} + |a_2|\frac{2(\Pi_{\mathrm{N}}^{(1)} + 1)}{\mathrm{N}!}\left(\frac{1}{2}\right)^{\mathrm{N}} \|\mathrm{u}^{(1+\mathrm{N})}\|_{\infty},
\end{aligned}$$

the time derivatives is computed precisely, so the bound of error of $\|\partial_\tau^\sigma(\mathrm{u} - \mathbf{I}_{\mathrm{N}}(\mathrm{u}))\|_{\infty}$, have the same order as $\|(\mathrm{u} - \mathbf{I}_{\mathrm{N}}(\mathrm{u}))\|_{\infty}$. Finally the error bound is given by

$$\mathfrak{E} \leq b_3 \|\mathrm{u}^{(\mathrm{N}+1)}\|_{\infty},$$

where b_3 can be obtained after the calculation of the coefficients of $\|\mathrm{u}^{(\mathrm{N}+1)}\|_{\infty}$. For 2-D models, interpolation operators based on the tensor product are used to calculate a similar error bound.

3.3 Numerical Inverse Laplace Transform Methods

We utilize the ILTMs for inversion of the solution obtained through CSCM in the Laplace space to time domain. The solution $\mathrm{u}(\bar{\boldsymbol{x}}, \tau)$ is approximated as follows:

$$\begin{aligned}
\mathrm{u}(\bar{\boldsymbol{x}}, \tau) &= \frac{1}{2\pi i}\int_{\vartheta - i\infty}^{\vartheta + i\infty} e^{\mathrm{s}\tau}\widehat{\mathrm{u}}(\bar{\boldsymbol{x}}, \mathrm{s})d\mathrm{s}, \\
&= \frac{1}{2\pi i}\int_{\mathscr{C}} e^{\mathrm{s}\tau}\widehat{\mathrm{u}}(\bar{\boldsymbol{x}}, \mathrm{s})d\mathrm{s}, \ \tau > 0,
\end{aligned} \tag{22}$$

where $\mathscr{C}$ is an appropriately selected integration contour of the left half complex plane linking $\vartheta - i\infty$ to $\vartheta + i\infty$. The integral presented in Eq. (22) is called the Bromwich integral. Various numerical algorithms are used in the literature to compute the integral in Eq. (22). As $\exp(\mathrm{s}\tau)$ on $\mathscr{C}$ is a very gradually decaying complex function, the numerical integration of the Eq. (22) is very tough to execute. The contour deformation [57] can be utilized to handle $\exp(\mathrm{s}\tau)$, in such a way that $\mathscr{C} : (\vartheta + i\infty, \vartheta - i\infty)$ is deformed to Hankel's contour that begins and ends in the half plane (to the left) such that $Re(\mathrm{s}) \longrightarrow -\infty$ at both ends, so $\exp(\mathrm{s}\tau)$ depreciates very fast and therefore making the integral in Eq. (22) convenient for the approximation by using the mid-point or the trapezoidal rule. This type of deformation can be established by the Cauchy's theorem in conformation to the reality that $\mathscr{C}$ resides in the neighborhood where $\widehat{\mathrm{u}}(\bar{\boldsymbol{x}}, \mathrm{s})$ is analytic. The Talbot approach

may fail if the transformed function $\widehat{\mathrm{u}}(\bar{\boldsymbol{x}}, \mathrm{s})$ have some singularities in the imaginary region of the complex plane. The appropriate contour will ensure the accuracy of the ILTMs. Several authors utilized different types of contours for the approximation of Eq. (22), however, we employ the optimal parabolic contour (C_P) and hyperbolic contour (C_H) presented in [58,60], which are discussed as follows.

3.3.1 Parabolic Contour (C_P)

The C_P proposed in [58] is given in parametric form as

$$\mathrm{s} = \gamma(1 + i\beta)^2 \tag{23}$$

For $\beta = \vartheta + i\nu$, where $\nu > 0$, $-\infty < \vartheta < \infty$, C_P is of the form

$$s(\vartheta) = \gamma\left((\nu - 1)^2 - \vartheta^2\right) - 2i\lambda\vartheta(\nu - 1), \tag{24}$$

where γ is an unknown parameter to be determined.

3.3.2 Hyperbolic Contour (C_H)

The parametric form of C_H proposed in [60] is of the form

$$s(\vartheta) = \alpha + \gamma - \alpha\sin(\rho - i\vartheta), \quad -\infty < \vartheta < \infty, \tag{25}$$

with $\gamma \geq 0$, and $\alpha > 0$, where α satisfies the relations $\frac{1}{2}\pi < \alpha < \pi$, and $0 < \rho < \alpha - \frac{1}{2}\pi$.

Now, using C_P or C_H in Eq. (22) we get

$$\mathrm{u}(\bar{\boldsymbol{x}}, \tau) = \frac{1}{2\pi i}\int_{-\infty}^{\infty} e^{\mathrm{s}(\vartheta)\tau}\widehat{\mathrm{z}}(\bar{\boldsymbol{v}}, \mathrm{s}(\vartheta))\mathrm{s}'(\vartheta)d\vartheta. \tag{26}$$

and the integral in Eq. (26) can be approximated using the trapezoidal rule, resulting in

$$\mathrm{u}_k(\bar{\boldsymbol{x}}, \tau) = \frac{k}{2\pi i}\sum_{j=-\mathrm{M}}^{\mathrm{M}} e^{\mathrm{s}(\vartheta_j)\tau}\widehat{\mathrm{z}}(\bar{\boldsymbol{v}}, \mathrm{s}(\vartheta_j))\mathrm{s}'(\vartheta_j), \quad \text{where} \quad \vartheta_j = jk. \tag{27}$$

3.4 Error Analysis of LT-CSCM

This section addresses the error analysis of the LT-CSCM. The Laplace transform is applied in the first step, which is inherently free of error. The CSCM is employed in the second step for approximating the solution of the transformed problem. The following theorem establishes the error bounds of the CSCM.

Theorem 4 (Theorem 5, pp. 48, [42]). *Let* $\mathrm{u}(\bar{\boldsymbol{x}}, \tau)$ *be a given function and for a sequence* $\{\bar{\boldsymbol{v}}_{\mathrm{m}}\}_{\mathrm{N}=1}^{\infty}$ *based on a set of interpolation nodes, the sequence* $\boldsymbol{x}_{\mathrm{m}} \to \varsigma$, *as* $m \to \infty$, *where* ς *is the density function, with associated potential* λ *defined by*

$$\lambda(\alpha) = \int_{-1}^{1} \varsigma(u)\log|\alpha - u|du,$$

where

$$\lambda_{[-1,1]} = \sup\{\lambda(u)\}, \quad u \in [-1, 1].$$

For every N, construct $\mathbb{P}_N$ a polynomial of the degree less than or equal to N which interpolate the $u(\bar{\boldsymbol{x}}, \tau)$ at $\{\boldsymbol{x}_m\}_{N=1}^{\infty}$. If $\exists\ \lambda_u > \lambda_{[-1,1]}$, where λ_u is a constant, such that $u(\bar{\boldsymbol{x}}, \tau)$ is differentiable at each point within the region defined by

$$\{\alpha \in \mathbb{C} : \lambda(\alpha) \leq \lambda_u\},$$

suppose for $k > 0$ a constant, such that $\forall \quad \bar{\boldsymbol{x}}$ and $\forall \quad N$,

$$|u(\bar{\boldsymbol{x}}, \tau) - \mathbb{P}_N| \leq k e^{-N(\lambda_u - \lambda_{[-1,1]})}.$$

The above estimate is valid for any order derivatives $(u^{\alpha}(\bar{\boldsymbol{x}}, \tau) - \mathbb{P}_N^{\alpha}$, where $\alpha \geq 1)$ with a new constant which will be still not dependent on N and u.

Finally, we employ the ILTMs in order to approximate the Eq. (27). While approximating Eq. (27) the convergence of the proposed scheme depends on $\mathscr{C}$, the set of optimal parameters and the domain $[\tau_0, T]$. The error analysis of the ILTMs is discussed in the following theorem.

The error of the C_P depends on error of trapezoidal-rule on real line. By comparison of Eqs. (26) and (27), let the integral is defined as

$$\mathfrak{I} = \int_{-\infty}^{\infty} \mathscr{Q}(\vartheta) d\vartheta,$$

the finite approximations are

$$\mathfrak{I}_k = k \sum_{k=-\infty}^{\infty} \mathscr{Q}(jk),$$

and the infinite approximations are

$$\mathfrak{I}_{k;M_P} = k \sum_{j=-M_P}^{M_P} \mathscr{Q}(jk).$$

The discretization error is given by $D_{err} = |\mathfrak{I} - \mathfrak{I}_k|$, and the truncation error is given by $T_{err} = |\mathfrak{I}_{k;M_P} - \mathfrak{I}_k|$. The following Theorem will establish the error estimate for C_P.

Theorem 5 [58]. *Let* $s = \vartheta + i\eta,\ \vartheta, \eta \in \mathbb{R}$. *Consider* $\mathscr{Q}(s)$ *is analytic in the strip* $\eta \in (-d, c)$, *for some* $d, c > 0$, *with* $\mathscr{Q}(s) \to 0$, *as* $|s| \to \infty$. *Let onsider positive constants* $\mathscr{G}_+, \mathscr{G}_-$, *then* $\mathscr{Q}(s)$ *must satisfy*

$$\int_{-\infty}^{\infty} |\mathscr{Q}(\vartheta + ir)| d\vartheta \leq \mathscr{G}_+, \quad \int_{-\infty}^{\infty} |\mathscr{Q}(\vartheta - iq)| d\vartheta \leq \mathscr{G}_-, \quad \forall\ 0 < r < c,\ 0 < q < d.$$

Then, we have

$$D_{err-} = \frac{\mathscr{G}_-}{exp\left(\frac{2\pi c}{k}\right) - 1}, \quad D_{err+} = \frac{\mathscr{G}_+}{exp\left(\frac{2\pi d}{k}\right) - 1}.$$

If $c = d, \mathscr{G}_+ = \mathscr{G}_- = \mathscr{G},$ and $\mathscr{Q}$ is real valued, then we get the following estimate

$$|\mathfrak{I} - \mathfrak{I}_k| \leq \frac{2\mathscr{G}}{exp\left(\frac{2\pi d}{k}\right) - 1}.$$

To get an estimation of D_{err}, Weideman and Trefethen [58] computed λ, and k by balancing D_{err} and T_{err} asymptotically with the parameter's optimal values. The parameter's optimal values for C_P are

$$k = \frac{1}{\mathscr{G}}(\sqrt{8\Upsilon+1}), \quad \Upsilon = \frac{T}{t_0}, \quad \gamma = \{(4\sqrt{8\Upsilon+1})T\}^{-1}(\pi\mathscr{G}).$$

The estimate of error is

$$Estimate_{M_P} = |\mathrm{u}(\bar{\boldsymbol{x}},\tau) - \mathrm{u}_k(\bar{\boldsymbol{x}},\tau)| = O\left(e^{-\left(2\pi\mathscr{G}\frac{1}{\sqrt{8\Upsilon+1}}\right)}\right). \tag{28}$$

The parameter $\mathscr{G}$ used in our numerical computations is defined by the relation $\mathrm{M_P} = \dfrac{2\mathscr{G}}{k}$, where $\mathrm{M_P}$ corresponds to the quadrature points and k the step of the quadrature rule.

Similarly, the estimation of the discretization error for the hyperbolic contour is presented in the following theorem.

Theorem 6 ([60], Theorem 2). *Let* $\mathrm{u}(\bar{\boldsymbol{x}},\tau)$ *be the solution of model (1), and let* $\widehat{\xi}$ *be analytic in the set* $\sum_\theta^\gamma$. *Set* $\alpha = 2\vartheta, \quad \vartheta \in (0,1]$, *and let* $\mathscr{C} \subset S_r \subset \sum_\theta^\gamma$ *is defined as* $\psi = \frac{\alpha}{\kappa T}$, *with* $\kappa = 1-\sin(\rho - r)$. *Suppose* $\mathrm{u}_k(\bar{\boldsymbol{x}},\tau)$ *be the approximation of Eq. (1) with* $k = \sqrt{\frac{\bar{r}}{\alpha \mathrm{M_H}}} \le \frac{\bar{r}}{\log 2}$. *Then, if* $\vartheta_0, \nu \ge 0$ *and* $\vartheta_0 + \frac{1}{2}\nu \ge \vartheta$, *we have, with* $C = C(\rho, r, \theta, \vartheta, \vartheta_0)$ *for* $0 \le \tau \le T$,

$$\|\mathrm{u}_k(\bar{\boldsymbol{x}},\tau) - \mathrm{u}(\bar{\boldsymbol{x}},\tau)\| \le C\mathscr{M}\alpha^{-1}T^\alpha e^{\gamma\tau}e^{-\sqrt{\bar{r}\alpha \mathrm{M_H}}}(\|\mathrm{u}_0\|_\vartheta + \|\widehat{\xi}\|_{\vartheta_0,\nu,\Sigma_\theta^\gamma}).$$

In the current work, we use the optimal contour of integration with the parameters given in Eq. (25) are suggested by McLean and Thomèe [60] as

$$\gamma = 1, \ \vartheta = \frac{1590}{10000}, \ r = \frac{2551}{10000}, \ \alpha = \frac{3180}{10000}, \ \rho = \frac{2835}{10000}, \ \text{with } \tau \in [0.5, 5],$$

and the error estimate is given as

$$\mathrm{Estimate}_{C_H} = |\mathrm{u}(\bar{\boldsymbol{x}},\tau) - \mathrm{z}_k(\bar{\boldsymbol{v}},\tau)| = O(\alpha^{-1}T^\alpha e^{\gamma\tau}e^{-\sqrt{\bar{r}\alpha \mathrm{M_H}}}).$$

4 Stability of Method

To analyze the stability of our numerical scheme, we express the system defined in (8) and (9) in its discrete form as follows:

$$\mathrm{T}\widehat{\mathrm{u}} = \mathbf{b}, \tag{29}$$

where T is a differentiation matrix obtained using the CSCM. The stability constant corresponding to system (29) is given by

$$\mathrm{Q} = \sup_{\widehat{\mathrm{u}}\neq 0} \frac{\|\widehat{\mathrm{u}}\|}{\|\mathrm{T}\widehat{\mathrm{u}}\|}, \tag{30}$$

The value of Q is finite using any type of discrete norms $\|\cdot\|$ on $\mathbb{R}^N$. Eq (30), we obtain the following inequality

$$\|\mathrm{T}\|^{-1} \le \frac{\|\widehat{\mathrm{u}}\|}{\|\mathrm{T}\widehat{\mathrm{u}}\|} \le \mathrm{Q}. \tag{31}$$

In terms of pseudoinverse $T^{\dagger}$ of T, we can write

$$\|T^{\dagger}\| = \sup_{\mu \neq 0} \frac{\|T^{\dagger}\mu\|}{\|\mu\|}. \tag{32}$$

Hence, we have the following bound:

$$\|T^{\dagger}\| \geq \sup_{\mu = T\widehat{u} \neq 0} \frac{\|T^{\dagger}T\widehat{u}\|}{\|T\widehat{u}\|} = \sup_{\widehat{u} \neq 0} \frac{\|\widehat{u}\|}{\|T\widehat{u}\|} = Q. \tag{33}$$

Eqs. (31) and (33) establish bounds for the constant Q. Although computing the pseudoinverse directly can be numerically expensive, it provides a theoretical guarantee for the stability of the system. In practice, for square matrices, MATLAB's `condest` function can be used to estimate the inverse norm $\|T^{-1}\|_{\infty}$. This leads to an estimate of Q as

$$Q \approx \frac{\texttt{condest}(T')}{\|T\|_{\infty}}. \tag{34}$$

This approach performs well for our differentiation matrix T, requiring only a small amount of computation. The bounds of the stability constant Q for the systems (8) and (9) corresponding to Example 1 and Example 2 are illustrated in Fig. 1a and Fig. 1b, respectively. It can be observed that $1 \leq Q \leq 1.14$, which show the stability constant Q is bounded by numbers not very large, which imply the numerical stability of the CSCM.

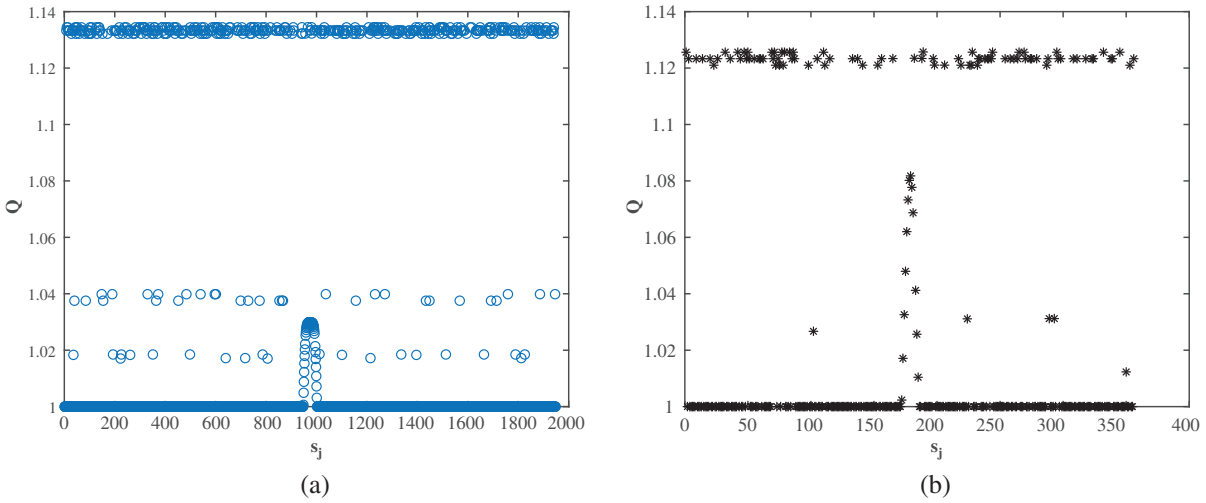

Figure 1: **(a)** The plot of the stability constant Q for Example 1, with N = 30, $M_H = 80$, and $\sigma = 0.6$ at $t = 1$. **(b)** The plot of the stability constant Q for Example 2, with N = 20, $M_P = 40$, and $\sigma = 0.5$ at $t = 1$

5 Numerical Experiments

We consider three different test examples to validate and check the efficiency of the LT-CSCM. The maximum absolute error norm is computed among the numerical solutions and the analytical solutions. The

error norm is defined as

$$Err_\infty = \max_{1\le j\le \mathrm{N}} |\mathrm{u}(\bar{\boldsymbol{x}}_j, \tau) - \mathrm{u}_k(\bar{\boldsymbol{x}}_j, \tau)|,$$

where u is the analytical solution and u_k is the approximate solution with the proposed method.

Example 1

Consider a 2D TFADE in Eq. (1) with exact solution $\mathrm{u}(x, y, \tau) = \tau^2 + x^2 + y^2$. The source term and initial boundary conditions are obtained from the exact solution. For simplicity we choose $a_1 = a_2 = 1$, and $(x, y, \tau) \in [-1, 1]^2 \times [0, 1]$. The numerical outcomes of the maximum absolute error norm via LT-CSCM with the parabolic and hyperbolic ILTMs utilizing the optimal values of the parameters defined in Theorem 5 and Theorem 6 using different numerical values of the parameters σ, N, $\mathrm{M_P}$, $\mathrm{M_H}$ at $\tau = 1$ are shown in Table 1 and for $\sigma = 0.5$, $\mathrm{M_H} = \mathrm{M_P} = 80$, N = 12 using different values of τ are shown in Table 2. We observe that with just N = 12, the error drops to 10^{-13}, demonstrating the exponential convergence of the Chebyshev spectral method. In contrast, other methods require more points to achieve comparable accuracy. Moreover, our method using the LT completes the computations in 4 to 22 seconds, while a time-stepping method takes more time due to iterative steps. The results of the proposed method are compared with those of the LT-based local RBF method. The comparison reveals that the proposed method achieves higher accuracy while requiring less number of points and computational time. The approximate solution of the test example 1 computed by LT-CSCM using $\sigma = 0.95$, N = 23, $\mathrm{M_H} = 120$ at $\tau = 1$ is depicted in Fig. 2a. Fig. 2b presents the Err_∞ error for the parabolic (C_P) and hyperbolic (C_H) contours as a function of M, computed using the LT-CSCM with $\sigma = 0.60$, $N = 10$, and $\tau = 1$, where C_P achieves high accuracy as compared to C_H. Fig. 3a shows Err_∞ vs. τ for both contours, with $N = 10$, $M_P = 80$, $M_H = 120$, and $\sigma = 0.60$, demonstrating C_H's superior accuracy. Similarly, Fig. 3b illustrates Err_∞ vs. the fractional order σ, using $N = 10$, $M_P = 80$, $M_H = 120$, and $\tau = 1$, with C_H consistently outperforming C_P. Fig. 4a,b display the error plots for varying values of τ. A slight increase in error is observed as τ increases, indicating a minor reduction in accuracy with larger τ. In the hyperbolic contour case, the error escalates with increasing τ for all values of M_H. Conversely, in the parabolic contour case, the error exhibits stability for $M_P < 65$, with a modest rise observed thereafter.

Table 1: Computed results of Err_∞ for test example 1 at $\tau = 1$

	σ = 0.45				σ = 0.95		
N	$\mathrm{M_P}$	Err_∞	CPU (s)	N	$\mathrm{M_H}$	Err_∞	CPU (s)
06	80	8.2601×10^{-14}	0.458728	12	80	5.5889×10^{-12}	4.570705
08		2.4114×10^{-13}	0.880215	14		5.8904×10^{-12}	7.698902
10		2.3537×10^{-13}	1.434758	16		5.6799×10^{-12}	12.740710
12		5.6044×10^{-13}	2.329241	18		6.0809×10^{-12}	22.604758
10	60	2.0307×10^{-11}	0.783448	14	60	1.7859×10^{-09}	3.302329
	70	2.4425×10^{-13}	1.094165		70	3.6660×10^{-09}	4.492414
	80	2.3537×10^{-13}	1.523354		80	4.1256×10^{-11}	5.902070
	90	2.4603×10^{-13}	1.825100		90	5.8904×10^{-12}	7.630492
06	80	5.3735×10^{-14}	0.474708	12	100	1.5765×10^{-13}	5.281663
08		1.3944×10^{-13}	0.878473	14		3.3573×10^{-13}	8.396366
10		3.3529×10^{-13}	2.225168	16		4.8139×10^{-13}	14.174648
12		3.5438×10^{-13}	2.705963	18		8.4110×10^{-13}	23.610341

(Continued)

Table 1 (continued)

	σ = 0.45				σ = 0.95		
N	M_P	Err_∞	CPU (s)	N	M_H	Err_∞	CPU (s)
10	60	2.0214×10^{-11}	0.747371	14	60	1.7859×10^{-09}	2.695916
	70	2.2249×10^{-13}	1.065972		70	3.6660×10^{-09}	3.809028
	80	3.3529×10^{-13}	1.454191		80	4.1256×10^{-11}	5.188223
	90	2.9354×10^{-13}	1.831423		90	5.7034×10^{-12}	6.592155
			[64]				
31	80	7.10×10^{-4}	276.273 092		60	7.32×10^{-4}	127.185 713

Table 2: Computed results of Err_∞ for test example 1 for various values of τ

	σ = 0.5, M_P = 80, N = 12		σ = 0.5, M_H = 80, N = 12	
τ	Err_∞	CPU (sec.)	Err_∞	CPU (sec.)
0.25	2.4647×10^{-13}	3.732022	5.5511×10^{-14}	8.825760
0.50	3.0020×10^{-13}	3.218428	1.0836×10^{-13}	8.701203
0.75	3.5172×10^{-13}	3.301843	1.3189×10^{-13}	8.666085
1.00	4.0723×10^{-13}	3.208423	1.1546×10^{-13}	8.708011
1.25	4.8272×10^{-13}	3.240704	1.9051×10^{-13}	8.771992
1.50	6.4171×10^{-13}	3.206866	2.3448×10^{-19}	8.635115
1.75	8.5443×10^{-13}	3.177401	2.6201×10^{-13}	8.740828
2.00	1.1502×10^{-12}	3.202478	3.5527×10^{-13}	8.623311

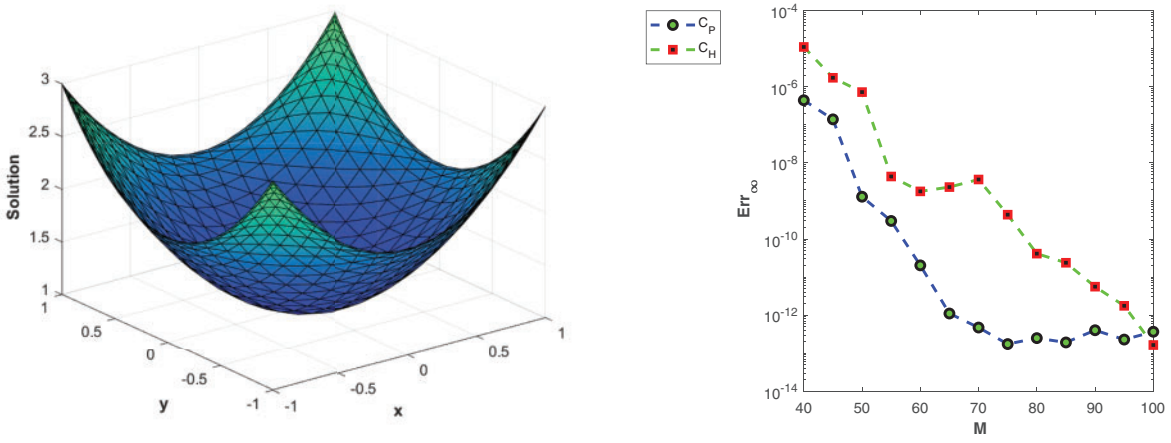

(a) (b)

Figure 2: **(a)** Numerical solution of test example 1 obtained by the proposed method. **(b)** Plots of Err_∞ vs. M computed by LT-CSCM using the two contours C_P(parabolic) and C_H(hyperbolic). The C_P yields more accurate results than the C_H, as evidenced by the reduced error across the range of nodes

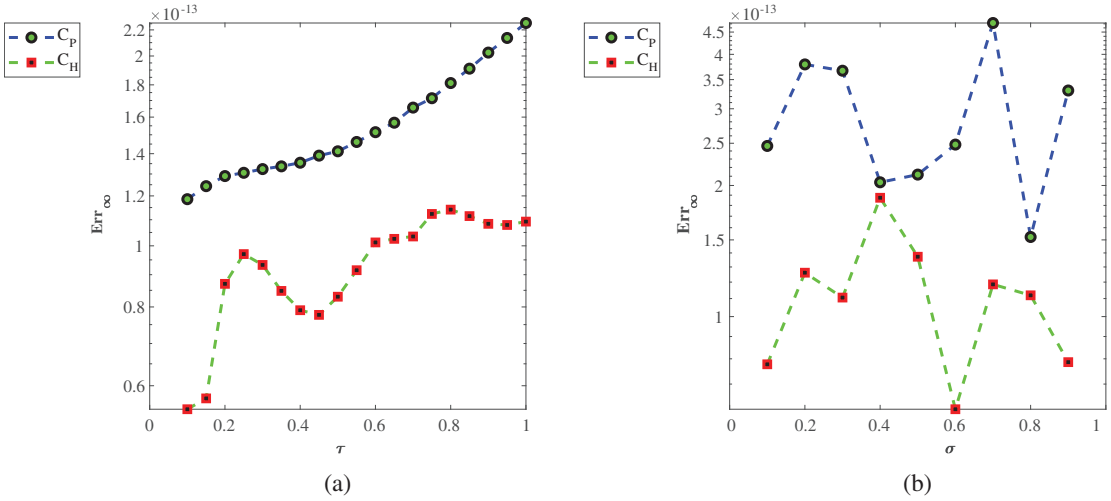

Figure 3: **(a)** The Plots shows Err_∞ as a function of τ computed by the LT-CSCM using the two contours C_P(parabolic) and C_H(hyperbolic). The C_H yields high accuracy, as evidenced by significantly lower error values across the evaluated time domain. **(b)** The Plots shows Err_∞ as a function of σ computed by LT-CSCM using the two contours C_P(parabolic) and C_H(hyperbolic). The results indicate that the C_H yields more accurate outcomes as compared to the C_P, as evidenced by the reduced error across the range of σ values

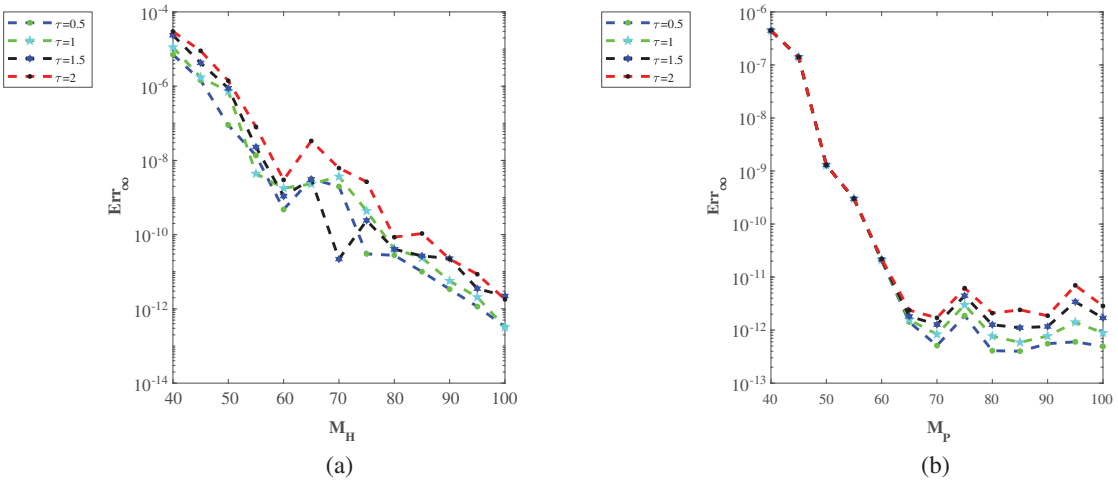

Figure 4: **(a)** We have plotted the error as a function of M_H for $\tau = [0.5, 1, 1.5, 2]$, with separate graphs for each case value of τ. This plot indicates a slight reduction in accuracy as τ increases, reflecting the influence of temporal evolution on the method's performance. **(b)** We have plotted the error as a function of M_P for $\tau = [0.5, 1, 1.5, 2]$, with separate graphs for each case value of τ. For $40 < M_P < 65$, the error remains relatively stable for all values of τ. However, for $M_P > 65$, the plots reveal a slight increase in error as τ increases, indicating a minor reduction in accuracy due to the influence of temporal evolution on the method's performance

Example 2

Consider a 2D TFADE defined in Eq. (1) with exact solution $u(x, y, \tau) = \tau^3 + \sin(x + y)$. The source term and initial boundary conditions are obtained from the exact solution. For simplicity we choose $a_1 = a_2 = 1$, and $(x, y, \tau) \in [-1, 1]^2 \times [0, 1]$. The numerical outcomes of the maximum absolute error norm via LT-CSCM with the parabolic and hyperbolic ILTMs utilizing the optimal values of the parameters defined in

Theorem 5 and Theorem 6 using different numerical values of the parameters σ, N, M_P, M_H at $\tau = 1$ are shown in Table 3 and for $\sigma = 0.5$, $M_H = M_P = 80$, $N = 12$ using different values of τ are shown in Table 4. The approximate solution of the test example 2 computed by LT-CSCM using $\sigma = 0.95$, $N = 23$, $M_H = 120$ at $\tau = 1$ is depicted in Fig. 5a. Fig. 5b displays Err_∞ error for the parabolic (C_P) and hyperbolic (C_H) contours as a function of the quadrature node count$M$, computed using the LT-CSCM with $\sigma = 0.60$, $N = 10$, and $\tau = 1$. The C_P contour yields superior accuracy compared to C_H. Fig. 6a presents Err_∞ vs. τ for both contours, with $N = 10$, $M_P = 80$, $M_H = 120$, and $\sigma = 0.60$, where C_P demonstrates greater precision. Likewise, Fig. 6b illustrates Err_∞ vs. the fractional order σ, using $N = 10$, $M_P = 80$, $M_H = 120$, and $\tau = 1$, with C_P consistently outperforming C_H. Fig. 7a,b display the error plots for varying values of τ. A slight increase in error is observed as τ increases, indicating a minor reduction in accuracy with larger τ. For the hyperbolic contour, larger τ values lead to a consistent error growth regardless of M_H. In contrast, the parabolic contour maintains near-constant error up to $M_P = 70$, beyond which a gradual increase is observed.

Table 3: Computed results of Err_∞ for test example 2 at $\tau = 1$

	$\sigma = 0.45$				$\sigma = 0.95$		
N	**M_P**	**Err_∞**	**CPU (s)**	**N**	**M_H**	**Err_∞**	**CPU (s)**
06	80	2.7632×10^{-06}	3.390702	06	80	2.7633×10^{-06}	0.761672
08		8.8751×10^{-09}	1.054598	08		8.8751×10^{-09}	1.385999
10		1.4140×10^{-11}	1.635748	10		2.6330×10^{-11}	2.367367
12		6.5681×10^{-13}	2.718997	12		2.0636×10^{-11}	3.727264
12	60	3.3851×10^{-09}	1.855325	12	60	8.9322×10^{-10}	2.006423
	70	9.8712×10^{-12}	1.953771		70	1.8334×10^{-09}	2.784457
	80	6.5681×10^{-13}	2.696487		80	2.0636×10^{-11}	3.698617
	90	3.8503×10^{-13}	3.506589		90	2.8182×10^{-12}	4.835735
06	80	2.8416×10^{-06}	0.553062	06	80	2.8416×10^{-06}	0.718420
08		9.2162×10^{-09}	0.988440	08		9.2161×10^{-09}	1.286288
10		1.4426×10^{-11}	1.587988	10		2.6456×10^{-11}	2.207315
12		2.4558×10^{-13}	2.704731	12		2.0658×10^{-11}	3.416381
12	60	3.3857×10^{-09}	1.488101	12	60	8.9324×10^{-10}	1.865004
	70	9.7549×10^{-12}	2.063635		70	1.8334×10^{-09}	2.872724
	80	2.4558×10^{-13}	2.746631		80	2.0658×10^{-11}	3.413514
	90	5.3868×10^{-13}	3.404533		90	2.8819×10^{-12}	4.358569

Table 4: Computed results of Err_∞ for test example 2 for various values of τ

	$\sigma = 0.5,\ M_P = 80,\ N = 12$		$\sigma = 0.5,\ M_H = 80,\ N = 12$	
τ	**Err_∞**	**CPU (sec.)**	**Err_∞**	**CPU (sec.)**
0.25	3.8958×10^{-13}	3.234866	1.0895×10^{-11}	4.411454
0.50	5.0648×10^{-13}	3.286405	1.3892×10^{-11}	6.046790
0.75	6.4793×10^{-13}	3.234721	1.4345×10^{-11}	4.479463
1.00	8.1668×10^{-13}	3.217594	2.0635×10^{-11}	4.384079
1.25	1.0147×10^{-12}	3.252007	3.8013×10^{-11}	4.438511

(Continued)

Table 4 (continued)

	$\sigma = 0.5,\ M_P = 80,\ N = 12$		$\sigma = 0.5,\ M_H = 80,\ N = 12$	
τ	Err_∞	CPU (sec.)	Err_∞	CPU (sec.)
1.50	1.2541×10^{-12}	3.249500	2.0234×10^{-11}	4.396462
1.75	1.5401×10^{-12}	3.245634	3.7421×10^{-11}	4.407512
2.00	1.9007×10^{-12}	3.435805	4.2814×10^{-11}	4.456666

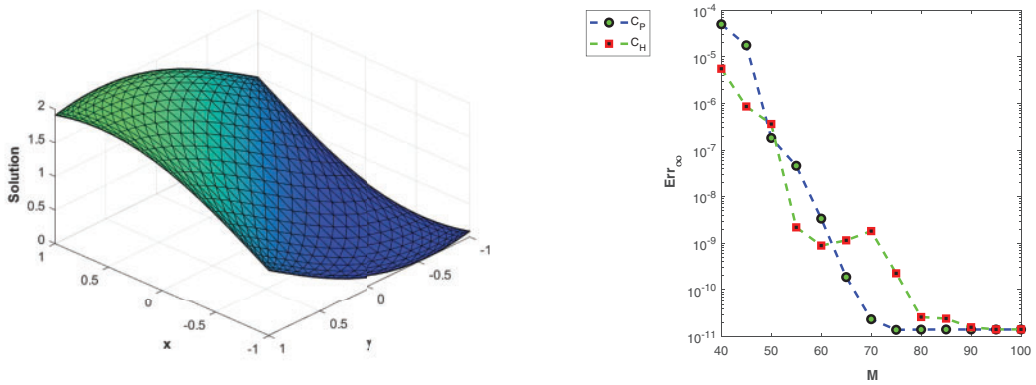

(a) (b)

Figure 5: **(a)** Numerical solution of test example 2 otained by the proposed method. **(b)** Plots of Err_∞ vs. M computed by LT-CSCM using the two contours C_P(parabolic) and C_H(hyperbolic). The C_P yields more accurate results than the C_H, as evidenced by the reduced error across the range of nodes

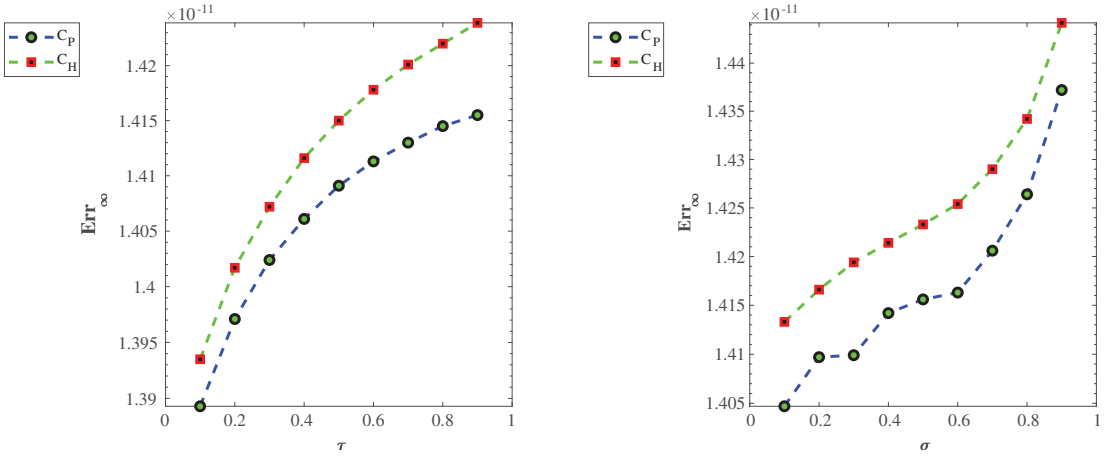

(a) (b)

Figure 6: **(a)** The Plots shows Err_∞ as a function of τ computed by the LT-CSCM using the two contours C_P(parabolic) and C_H(hyperbolic). The C_P contour consistently achieves higher accuracy, as demonstrated by substantially lower error values across the evaluated time domain. **(b)** The Plots shows Err_∞ as a function of σ computed by LT-CSCM using the two contours C_P(parabolic) and C_H(hyperbolic). The results indicate that the C_P contour, with significantly reduced errors across the range of σ values, indicating superior accuracy

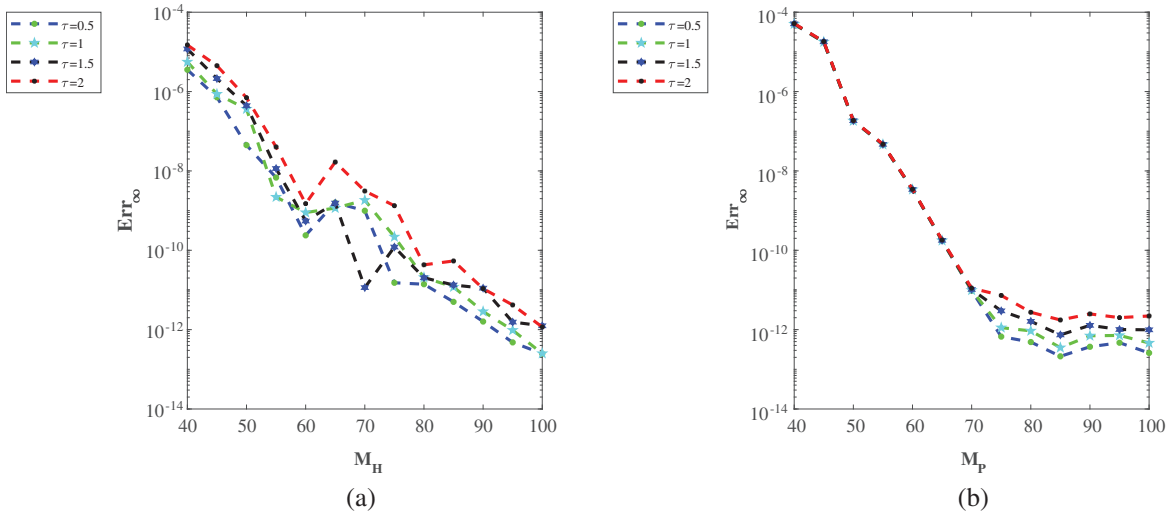

Figure 7: **(a)** We have plotted the error as a function of M_H for $\tau = [0.5, 1, 1.5, 2]$, with separate graphs for each case value of τ. This plot indicates a slight reduction in accuracy as τincreases, reflecting the influence of temporal evolution on the method's performance. **(b)** We have plotted the error as a function of M_P for $\tau = [0.5, 1, 1.5, 2]$, with separate graphs for each case value of τ. For $40 < M_P < 70$, the error remains relatively stable for all values of τ. However, for $M_P > 70$, the plots reveal a slight increase in error as τ increases, indicating a minor reduction in accuracy due to the influence of temporal evolution on the method's performance

Example 3

Consider a 2D TFADE in Eq. (1) with exact solution $u(x, y, \tau) = (1 + \tau^3 + \tau^4)\cos(\frac{\pi}{2}x)\cos(\frac{\pi}{2}y)$. The source term and initial boundary conditions are obtained from the exact solution. For simplicity we choose $a_1 = a_2 = 1$, and $(x, y, \tau) \in [-1, 1]^2 \times [0, 1]$. The numerical outcomes of the maximum absolute error norm via LT-CSCM with the parabolic and hyperbolic ILTMs utilizing the optimal values of the parameters defined in Theorem 5 and Theorem 6 using different numerical values of the parameters σ, N, M_P, M_H at $\tau = 1$ are shown in Table 5 and for $\sigma = 0.5$, $M_H = M_P = 80$, $N = 12$ using different values of τ are shown in Table 6. The approximate solution of the test example 3 computed by LT-CSCM using $\sigma = 0.95$, $N = 23$, $M_H = 120$ at $\tau = 1$ is depicted in Fig. 8a. Fig. 8b illustrates the L_∞ error (Err_∞) for the parabolic (C_P) and hyperbolic (C_H) contours as a function of$M$, computed using the LT-CSCM with $\sigma = 0.60$, $N = 10$, and $\tau = 1$. The C_H contour performs better than C_P. Fig. 9a displays Err_∞ vs. τ, with $N = 10$, $M_P = 80$, $M_H = 120$, and $\sigma = 0.60$, where C_P and C_H have produced almost similar results. Similarly, Fig. 9b presents Err_∞ vs. σ, with $N = 10$, $M_P = 70$, $M_H = 60$, and $\tau = 1$, with C_H outperforming C_P. Fig. 10a,b display the error plots for varying values of τ. A slight increase in error is observed as τ increases, indicating a minor reduction in accuracy with larger τ. With the hyperbolic contour, the error rises steadily as τ increases for all M_H. For the parabolic contour, however, the error remains largely unchanged until $M_P = 80$, after which it gradually increases.

Table 5: Computed results of Err_∞ for test example 3 at $\tau = 1$

	σ = 0.45				σ = 0.95		
N	M_P	Err_∞	CPU (s)	N	M_H	Err_∞	CPU (s)
06	80	7.2419×10^{-05}	0.635034	06	80	7.2419×10^{-05}	0.789779
08		4.3969×10^{-05}	1.041039	08		4.3967×10^{-07}	1.520031

(Continued)

Table 5 (continued)

	σ = 0.45				σ = 0.95		
N	**M_P**	**Err_∞**	**CPU (s)**	**N**	**M_H**	**Err_∞**	**CPU (s)**
10		1.5267×10^{-09}	1.731705	10		1.5456×10^{-09}	2.339859
12		7.9465×10^{-12}	2.683817	12		2.0355×10^{-11}	3.832206
12	60	4.1473×10^{-07}	1.408286	12	60	8.8889×10^{-10}	2.106545
	70	1.3362×10^{-09}	2.022943		70	1.8291×10^{-09}	2.877898
	80	7.9465×10^{-12}	2.757916		80	2.0355×10^{-11}	3.822222
	90	4.5706×10^{-12}	3.398950		90	5.3051×10^{-12}	4.890334
06	80	6.7846×10^{-05}	0.687953	06	80	6.7846×10^{-05}	0.742059
08		4.1668×10^{-07}	1.020232	08		4.1666×10^{-07}	1.333140
10		1.4685×10^{-09}	1.722290	10		1.4875×10^{-09}	2.200380
12		7.7858×10^{-12}	2.705505	12		2.0430×10^{-11}	3.429313
12	60	4.1473×10^{-07}	1.409197	12	60	8.8905×10^{-10}	1.897165
	70	1.3363×10^{-09}	2.067497		70	1.8293×10^{-09}	2.618052
	80	7.7858×10^{-12}	2.706083		80	2.0430×10^{-11}	3.453511
	90	4.4067×10^{-12}	3.463687		90	5.3770×10^{-12}	4.372541

Table 6: Computed results of Err_∞ for test example 3 for various values of τ

	σ = 0.5, M_P = 80, N = 12		σ = 0.5, M_H = 80, N = 12	
τ	**Err_∞**	**CPU (sec.)**	**Err_∞**	**CPU (sec.)**
0.25	4.9019×10^{-12}	3.341849	1.0193×10^{-11}	4.378416
0.50	5.2023×10^{-12}	3.412732	1.5584×10^{-11}	4.331457
0.75	6.0569×10^{-12}	3.323900	1.6822×10^{-11}	4.335437
1.00	7.9439×10^{-12}	3.391502	2.0360×10^{-11}	4.350298
1.25	1.1470×10^{-11}	3.389320	4.5721×10^{-11}	4.499091
1.50	1.7392×10^{-11}	3.359923	2.6373×10^{-11}	4.344852
1.75	2.6596×10^{-11}	3.433501	5.9959×10^{-11}	4.366634
2.00	4.0110×10^{-11}	3.395691	7.8646×10^{-11}	4.374096

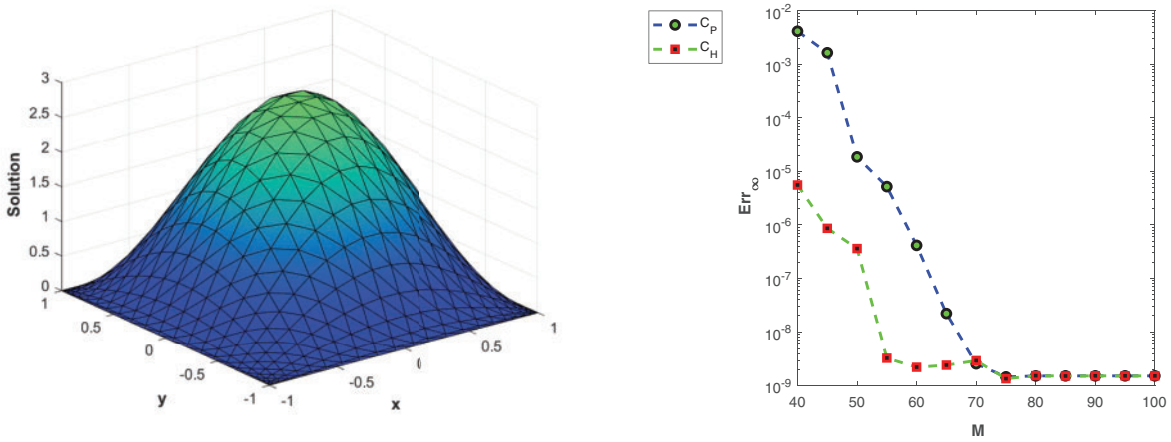

Figure 8: **(a)** Numerical solution of test example 3 obtained by the proposed method. **(b)** Plots of Err_∞ vs. M computed by LT-CSCM using the two contours C_P(parabolic) and C_H(hyperbolic). The C_H yields more accurate results than the C_P, as evidenced by the reduced error across the range of node

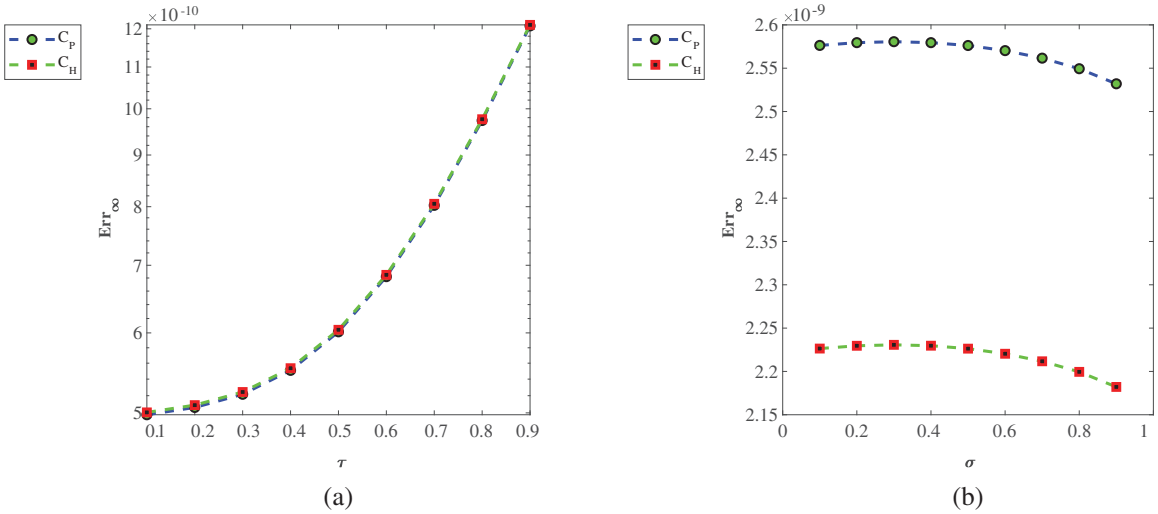

Figure 9: **(a)** The Plots shows Err_∞ as a function of τ computed by the LT-CSCM using the two contours C_P(parabolic) and C_H(hyperbolic). The curves for both contours overlap closely, indicating comparable accuracy across the evaluated τ range, with negligible differences in error. **(b)** The Plots shows Err_∞ as a function of σ computed by LT-CSCM using the two contours C_P(parabolic) and C_H(hyperbolic). The results indicate that the C_H contour, with significantly reduced errors across the range of σ values, indicating superior accuracy

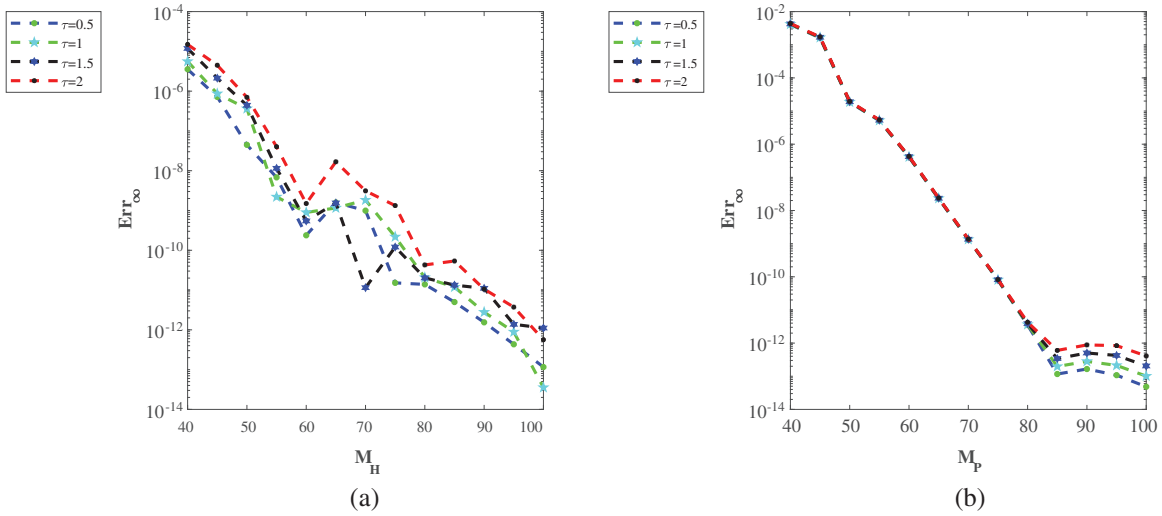

Figure 10: **(a)** We have plotted the error as a function of M_H for $\tau = [0.5, 1, 1.5, 2]$, with separate graphs for each case value of τ. This plot indicates a slight reduction in accuracy as τincreases, reflecting the influence of temporal evolution on the method's performance. **(b)** We have plotted the error as a function of M_P for $\tau = [0.5, 1, 1.5, 2]$, with separate graphs for each case value of τ. For $40 < M_P < 80$, the error remains relatively stable for all values of τ. However, for $M_P > 80$, the plots reveal a slight increase in error as τ increases, indicating a minor reduction in accuracy due to the influence of temporal evolution on the performance of the method

6 Conclusion

In this study, we developed a LT-CSCM to solve time-fractional advection-diffusion equations including the AB derivative with high accuracy and computational efficiency. By integrating the LT with the CSCM, our approach combines the advantages of both approaches: the Laplace transform eliminates time-stepping complexities, ensuring exact temporal discretization, while the CSCM, utilizing Lagrange polynomials-based on Chebyshev nodes, achieves exponential convergence in the spatial domain with minimal nodes. This combination results in low computational cost and high accuracy, as demonstrated by the excellent agreement between our numerical results and exact solutions across various test cases. Despite these advantages, we acknowledge certain limitations. The CSCM's reliance on global basis functions can pose challenges for problems involving irregular geometries or complex boundary conditions, where local methods might be more adaptable. Furthermore, the global nature of the approach may limit its adaptability to very large-scale problems. To revert solutions from the Laplace domain to the time domain, we employed a numerical inverse Laplace transform, which maintained stability and accuracy throughout. Overall, the LT-CSCM proves to be a robust and efficient tool for time-fractional advection-diffusion problems, with the potential for further refinement to address complex geometries and broader applications. As a future direction, we aim to extend the proposed LT-CSCM framework to solve multi-dimensional time-fractional problems and to compare the performance and accuracy of the method when applied to different types of fractional derivatives, including the modified Atangana-Baleanu derivative. This will enable a deeper understanding of the method's adaptability and effectiveness across various fractional models and more realistic physical phenomena.

Acknowledgement: The authors extend their appreciation to the Deanship of Research and Graduate Studies at King Khalid University for funding this work through Large Research Project under grant number RGP2/174/46.

Funding Statement: The authors extend their appreciation to the Deanship of Research and Graduate Studies at King Khalid University for funding this work through Large Research Project under grant number RGP2/174/46.

Author Contributions: Kamran: Conceptualization, methodology, validation, investigation, writing—original draft, visualization, supervision, writing—review and editing. Farman Ali Shah: methodology, software, writing—original draft, data curation, writing—review and editing. Kallekh Afef: validation, formal analysis, investigation, writing—review and editing, project administration. J. F. Gómez-Aguilar: investigation, data curation, visualization, writing—review and editing. Salma Aljawi: validation, investigation, formal analysis, resources. Ioan-Lucian Popa: formal analysis, investigation, visualization, funding acquisition. All authors reviewed the results and approved the final version of the manuscript.

Availability of Data and Materials: All the data produced or examined in this study are provided within this article.

Ethics Approval: There does not exist any ethical issue regarding this work.

Conflicts of Interest: The authors declare no conflicts of interest to report regarding the present study.

References

1. Sun H, Zhang Y, Baleanu D, Chen W, Chen Y. A new collection of real world applications of fractional calculus in science and engineering. Commun Nonlinear Sci Numer Simul. 2018;64:213–31. doi:10.1016/j.cnsns.2018.04.019.
2. Podlubny I. Fractional differential equations. San Diego, CA, USA: Academic Press; 1998.
3. Abdeljawad T, Baleanu D. Discrete fractional differences with nonsingular discrete Mittag-Leffler kernels. Adv Differ Equ. 2016;2016:1–18. doi:10.1186/s13662-016-0949-5.
4. Jena SR, Sahu I. A novel approach for numerical treatment of traveling wave solution of ion acoustic waves as a fractional nonlinear evolution equation on Shehu transform environment. Phys Scr. 2023;98(8):085231. doi:10.1088/1402-4896/ace6de.
5. Li C, Guo H, Tian X, He T. Generalized thermoelastic diffusion problems with fractional order strain. Eur J Mech-A/Solids. 2019;78:103827. doi:10.1016/j.euromechsol.2019.103827.
6. Kilbas AA, Srivastava HM, Trujillo JJ, Theory and applications of fractional differential equations. Vol. 204. Amsterdam, The Netherland: Elsevier; 2006.
7. Caputo M, Fabrizio M. A new definition of fractional derivative without singular kernel. Prog Fract Differ Appl. 2015;1(2):73–85. doi:10.12785/pfda/010201.
8. Atangana A, Baleanu D. New fractional derivatives with nonlocal and non-singular kernel: theory and application to heat transfer model. Therm Sci. 2016;20(2):763. doi:10.2298/TSCI160111018A.
9. Hristov J. On the Atangana-Baleanu derivative and its relation to the fading memory concept: the diffusion equation formulation. Fractional derivatives with mittag-leffler kernel: trends and applications in science and engineering. 1st ed. Cham, Switzerland: Springer; 2019. p. 175–93. doi:10.32604/iasc.2023.032883.
10. Zlatev Z, Berkowicz R, Prahm LP. Implementation of a variable stepsize variable formula method in the time-integration part of a code for treatment of long-range transport of air pollutants. J Comput Phys. 1984;55(2):278–301. doi:10.1016/0021-9991(84)90007-X.
11. Bakunin OG. Turbulence and diffusion: scaling vs. equations. Berlin/Heidelberg, Germany: Springer Science & Business Media; 2008. doi:10.1007/978-3-540-68222-6.
12. Sun L, Qiu H, Wu C, Niu J, Hu BX. A review of applications of fractional advection-dispersion equations for anomalous solute transport in surface and subsurface water. Wiley Interdiscip Rev: Water. 2020;7(4):e1448. doi:10.1002/wat2.1448.
13. Da Silva JRD, Xavier PHF, Moreira DM. Near-field atmospheric dispersion modeling: a new approach for the two-dimensional steady-state advection-diffusion equation using fractal derivative. Pure Appl Geophys. 2025;182(1):223–33. doi:10.1007/s00024-024-03624-8.
14. Budinski L. Solute transport in shallow water flows using the coupled curvilinear Lattice Boltzmann method. J Hydrol. 2019;573:557–67. doi:10.1016/j.jhydrol.2019.03.094.
15. Gupta R, Kumar S. Chebyshev spectral method for the variable-order fractional mobile-immobile advection-dispersion equation arising from solute transport in heterogeneous media. J Eng Math. 2023;142(1):1–28. doi:10.1007/s10665-023-10288-1.

16. Zhang H, Misbah C. Lattice Boltzmann simulation of advection-diffusion of chemicals and applications to blood flow. Comput Fluids. 2019;187:46–59. doi:10.1016/j.compfluid.2019.04.018.
17. Moranda A, Cianci R, Paladino O. Analytical solutions of one-dimensional contaminant transport in soils with source production-decay. Soil Systems. 2018;2(3):40. doi:10.3390/soilsystems2030040.
18. Sanskrityayn A, Kumar N. Analytical solution of advection-diffusion equation in heterogeneous infinite medium using Green's function method. J Earth Sys Sci. 2016;125:1713–23. doi:10.1007/s12040-016-0756-0.
19. Avci D, Yetim A. Analytical solutions to the advection-diffusion equation with the Atangana-Baleanu derivative over a finite domain. Balikesir Universitesi Fen Bilimleri Enstitusu Dergisi. 2018;20(2):382–95. doi:10.25092/baunfbed.487074.
20. Mirza IA, Vieru D. Fundamental solutions to advection-diffusion equation with time-fractional Caputo-Fabrizio derivative. Comput Math Appl. 2017;73(1):1–10. doi:10.1016/j.camwa.2016.09.026.
21. Umer A, Abbas M, Shafiq M, Abdullah FA, De la Sen M, Abdeljawad T. Numerical solutions of Atangana-Baleanu time-fractional advection diffusion equation via an extended cubic B-spline technique. Alex Eng J. 2023;74:285–300. doi:10.1016/j.aej.2023.05.028.
22. Fazio R, Jannelli A, Agreste S. A finite difference method on non-uniform meshes for time-fractional advection-diffusion equations with a source term. Appl Sci. 2018;8(6):960. doi:10.3390/app8060960.
23. Ahmed S, Jahan S, Nisar KS. Haar wavelet based numerical technique for the solutions of fractional advection diffusion equations. J Math Comput Sci. 2024;34(3):217–33. doi:10.22436/jmcs.034.03.02.
24. Kamran, Shah FA, Aly WHF, Aksoy H, Alotaibi FM, Mahariq I. Numerical inverse laplace transform methods for advection-diffusion problems. Symmetry. 2022;14(12):2544. doi:10.3390/sym14122544.
25. Pareek N, Gupta A, Agarwal G, Suthar DL. Natural transform along with HPM technique for solving fractional ADE. Adv Math Phys. 2021;2021(1):9915183. doi:10.1155/2021/9915183.
26. Chawla MM, Al-Zanaidi MA, Al-Aslab M. Extended one-step time-integration schemes for convection-diffusion equations. Comput Math Appl. 2000;39(3–4):71–84. doi:10.1016/S0898-1221(99)00334-X.
27. Liu J, Li X, Hu X. A RBF-based differential quadrature method for solving two-dimensional variable-order time fractional advection-diffusion equation. J Comput Phys. 2019;384:222–38. doi:10.1016/j.jcp.2018.12.043.
28. Nguyen H, Reynen J. A space-time least-square finite element scheme for advection-diffusion equations. Comput Methods Appl Mech Eng. 1984;42(3):331–42. doi:10.1016/0045-7825(84)90012-4.
29. Cunha CLN, Carrer JAM, Oliveira MF, Costa VL. A study concerning the solution ofadvection-diffusion problems by the Boundary Element Method. Eng Anal Bound Elem. 2016;100(65):79–94. doi:10.1016/j.enganabound.2016.01.002.
30. Sweilam NH, El-Sayed AAE, Boulaaras S. Fractional-order advection-dispersion problem solution via the spectral collocation method and the non-standard finite difference technique. Chaos Solitons Fractals. 2021;144:110736. doi:10.1016/j.chaos.2021.110736.
31. Yin F, Song J, Lu F. A coupled method of Laplace transform and Legendre wavelets for nonlinear Klein-Gordon equations. Math Methods Appl Sci. 2014;37(6):781–92. doi:10.1002/mma.2834.
32. Soares D Jr, Mansur WJ. An efficient time-domain BEM/FEM coupling for acoustic-elastodynamic interaction problems. Comput Model Eng Sci. 2005;8(2):153–64. doi:10.3970/cmes.2005.008.153.
33. Yin F, Song J, Lu F, Leng H. A coupled method of Laplace transform and Legendre wavelets for Lane-Emden-type differential equations. J Appl Math. 2012;2012(1):163821. doi:10.1155/2012/163821.
34. Khan Y, Faraz N, Kumar S, Yildirim A. A coupling method of homotopy perturbation and Laplace transformation for fractional models. Univ Politehnica Bucharest Scientific Bulletin Series A Appl Math Phy. 2012;74(1):57–68.
35. Joujehi AS, Derakhshan MH, Marasi HR. An efficient hybrid numerical method for multi-term time fractional partial differential equations in fluid mechanics with convergence and error analysis. Commun Nonlinear Sci Numer Simul. 2022;114:106620. doi:10.1016/j.cnsns.2022.106620.
36. Hafez RM, Youssri YH. Review on Jacobi-Galerkin spectral method for linear PDEs in applied mathematics. Contemp Math. 2024;5(2):2051–88. doi:10.37256/cm.5220244768.

37. Lim KM, Li H. A coupled boundary element/finite difference method for fluid-structure interaction with application to dynamic analysis of outer hair cells. Comput Struct. 2007;85(11–14):911–22. doi:10.1016/j.compstruc.2007.01.003.
38. Kamran, Khan S, Alhazmi SE, Alotaibi FM, Ferrara M, Ahmadian A. On the numerical approximation of mobile-immobile advection-dispersion model of fractional order arising from solute transport in porous media. Fractal Fract. 2022;6(8):445. doi:10.3390/fractalfract6080445.
39. Sahu I, Jena SR. An efficient technique for time fractional Klein-Gordon equation based on modified Laplace Adomian decomposition technique via hybridized Newton-Raphson Scheme arises in relativistic fractional quantum mechanics. Partial Differ Equ Appl Math. 2024;10:100744. doi:10.1016/j.padiff.2024.100744.
40. Boyd JP. Chebyshev and fourier spectral methods. 2nd ed. North Chelmsford, MA, USA: Courier Corporation; 2001.
41. Welfert BD. Generation of pseudospectral differentiation matrices I. SIAM J Numer Anal. 1997;34(4):1640–57. doi:10.1137/S0036142993295545.
42. Trefethen LN. Spectral methods in MATLAB (Software, Environments, and Tools). Philadelphia, PA, USA: SIAM; 2000.
43. Bueno-Orovio A, Perez-Garcia VM, Fenton FH. Spectral methods for partial differential equations in irregular domains: the spectral smoothed boundary method. SIAM J Sci Comput. 2006;28(3):886–900. doi:10.1137/040607575.
44. Khader MM, Saad KM. A numerical approach forsolving the fractional Fisher equation using Chebyshev spectral collocation method. Chaos Solitons Fractals. 2018;110:169–77. doi:10.1016/j.chaos.2018.03.018.
45. Bayrak MA, Demir A, Ozbilge E. Numerical solution of fractional diffusion equation by Chebyshev collocation method and residual power series method. Alex Eng J. 2020;59:4709–17. doi:10.1016/j.aej.2020.08.033.
46. Shokri A, Mirzaei S. A pseudo-spectral based method for time-fractional advection-diffusion equation. Comput Methods Differ Equ. 2020;8:454–67. doi:10.22034/cmde.2020.29307.1414.
47. Tohidi E. Application of Chebyshev collocation method for solving two classes of non-classical parabolic PDEs. Ain Shams Eng J. 2015;6(1):373–9. doi:10.1016/j.asej.2014.10.021.
48. Khater AH, Temsah RS, Hassan M. A Chebyshev spectral collocation method for solving Burger's-type equations. J Comput Appl Math. 2008;222(2):333–50. doi:10.1016/j.cam.2007.11.007.
49. Li Z, Chen X, Qiu J, Xia T. A novel Chebyshev-collocation spectral method for solving the transport equation. J Ind Manag Optim. 2021;17(5):2519–26. doi:10.3934/jimo.2020080.
50. Rongpei Z, Mingjun L, Xijun Y. An efficient Chebyshev spectral collocation method for the solution of reaction diffusion systems. J Numer Methods Comput Appl. 2017;38(4):271–81. doi:10.12288/szjs.2017.4.271.
51. Fu ZJ, Chen W, Yang HT. Boundary particle method for Laplace transformed time fractional diffusion equations. J Comput Phys. 2013;235:52–66. doi:10.1016/j.jcp.2012.10.018.
52. Diethelm K. The analysis of fractional differential equations: an application-oriented exposition using differential operators of caputo type. Berlin, Germany: Springer; 2010.
53. Mainardi F. Fractional calculus and waves in linear viscoelasticity: an introduction to mathematical models. Singapore: World Scientific; 2010.
54. Gorenflo R, Mainardi F, Moretti D, Pagnini G, Paradisi P. Discrete random walk models for space-time fractional diffusion. Chem Phys. 2002;284(1–2):521–41. doi:10.1016/S0301-0104(02)00714-0.
55. De Hoog FR, Knight JH, Stokes AN. An improved method for numerical inversion of Laplace transforms. SIAM J Sci Stat Comput. 1982;3(3):357–66. doi:10.1137/0903022.
56. Stehfest H. Algorithm 368: numerical inversion of Laplace transforms [D5]. Commun ACM. 1970;13(1):47–9. doi:10.1145/361953.361969.
57. Talbot A. The accurate numerical inversion of Laplace transforms. IMA J Applied Math. 1979;23(1):97–120. doi:10.1093/imamat/23.1.97.
58. Weideman J, Trefethen L. Parabolic and hyperbolic contours for computing the Bromwich integral. Math Comput. 2007;76(259):1341–56. doi:10.1090/S0025-5718-07-01945-X.

59. Weeks WT. Numerical inversion of Laplace transforms using Laguerre functions. J ACM (JACM). 1966;13(3):419–29. doi:10.1145/321341.321351.
60. McLean W, Thomèe V. Numerical solution via Laplace transforms of a fractional order evolution equation. J Integral Equ Appl. 2010:57–94. doi:10.1216/JIE-2010-22-1-57.
61. Verma P, Kumar M. New existence, uniqueness results for multi-dimensional multi-term Caputo time-fractional mixed sub-diffusion and diffusion-wave equation on convex domains. J Appl Analysis Comput. 2021;11:1455–80. doi:10.11948/20200217.
62. Baltensperger R, Trummer MR. Spectral differencing with a twist. SIAM J Sci Comput. 2003;24(5):1465–87. doi:10.1137/S1064827501388182.
63. Börm S, Grasedyck L, Hackbusch W. Introduction to hierarchical matrices with applications. Eng Anal Bound Elem. 2003;27(5):405–22. doi:10.1016/S0955-7997(02)00152-2.
64. Kamran, Ahmadian A, Salahshour S, Salimi M. A robust numerical approximation of advection diffusion equations with nonsingular kernel derivative. Phys Scr. 2021;96(12):124015. doi:10.1088/1402-4896/ac1ccf.